Oceanologia, Vol. 66, No. 3, 2024

https://doi.org/10.5697/ECMX9318

Monsoonal patterns of wave reflection from rubble mound breakwater of Chabahar Bay

Seyed Masoud Mahmoudof*[,1], Amin Eyhavand-Koohzadi[1,2], Ali Khosh Kholgh*[,1]

Abstract
This paper presents the results of a one-year field study on the monsoonal reflective response of the rubble mound breakwater (RMB) of Chabahar Bay, located on the northern coast of the Gulf of Oman, Iran. Measurements show that, in general, the correlation between the reflection coefficient and Iribarren number during the winter monsoon period is more remarkable than that of the summer monsoon period. The difference in wave reflection behavior during monsoonal periods is mainly due to the energy proportion of incoming sea and swell waves. Various characteristic wave periods by means of power- and hyperbolic-law prediction functions are explored to enhance the wave reflection prediction, highlighting the significant performance of negative-moment spectral periods T_{m-1} and T_{m-2} compared with peak and mean spectral periods. Statistical comparison of the performance of T_{m-1} and T_{m-2} shows that T_{m-2} considerably improves the prediction accuracy for moderated energy waves with bimodal sea and swell climates originating from different directions in the winter monsoon and pre-summer monsoon months. However, the prediction improvement is insignificant for unimodal energetic waves observed during the summer monsoon months. Generally, using T_{m-2} increases the accuracy of the preexisting equations in predicting the observations of this study.

Keywords
Field measurements; Permeable structure; Bimodal wave climate; Seasonal variation; Shahid-Beheshti Port; Makran

[1] *Iranian National Institute for Oceanography and Atmospheric Sciences (INIOAS), Tehran, Iran*
[2] *School of Civil Engineering, College of Engineering, University of Tehran, Tehran, Iran*
***Correspondence**: m_mahmoudof@inio.ac.ir (S.M. Mahmoudof), a_khosh@inio.ac.ir (A. Khosh Kholgh)

Received: 30 April 2024; **revised:** 29 June 2024; **accepted**: 3 July 2024

1. Introduction

Chabahar Bay, situated along the Makran coastline north of the Gulf of Oman, is a strategic port pivotal to trade, connectivity, economic growth, and regional stability in the southern part of Iran. The rubble mound breakwater (RMB) of Shahid-Beheshti commercial port plays a crucial role in mitigating coastal wave hazards, further supporting these activities through Chabahar Bay. The Gulf of Oman is subject to significant seasonal changes in wind direction and wave cycles that influence its wave climate, environment, and economic activities. These different atmospheric regimes are primarily driven by the seasonally reversing Indian Ocean monsoon wind system (Sinha et al., 2020; Shamji, 2021; Smitha et al., 2023). Prevailing winds typically originate from the southwest between May and August, marking the summer monsoon season, and from the northeast between November and February for the winter monsoon period (Shankar et al., 2002; Lahiri and Vissa, 2022; Karnan and Gautham, 2023). The intermonsoonal months of March-April and September-October are pre-summer monsoon and post-summer monsoon periods, respectively, which exhibit relatively shifting wind patterns (Vinod Kumar et al., 2014; Smith et al., 2020; Krishna et al., 2023). This annual monsoon cycle brings about changes in wave energy and direction, which have implications for the performance of coastal defense structures, coastal erosion, and navigation.

Saket and Etemad-Shahidi (2012) explored the Indian Ocean monsoons to investigate wave power potential along the Iranian coasts of the Gulf of Oman. They revealed that the most energetic waves in Chabahar Bay originate from the southwest monsoon between June and August, with significant wave heights ranging from 1 to 3 m and periods between 4 and 8 s, primarily in the southeast direction. However, they did not explain how southwest winds could generate significant waves in the southeast direction. Amrutha et al. (2015) examined wave characteristics before, during, and after the onset of the Indian summer monsoon using data collected by buoys located off the central west coast of India. Their research revealed significant changes in the wave field during the monsoonal periods, with mean significant wave height increasing from 0.7–0.9 m before the monsoon to 2.4–2.6 m during its domination. Addi-

tionally, the peak wave period in one day varied up to 15 s before the monsoon due to the influence of the sea-land breeze circulation. Sreelakshmi and Bhaskaran (2020) presented a comprehensive analysis of 41 years of ERA-5 wind-wave data (1979–2019) in the Indian Ocean, including long-term trends, inter-annual, and inter-seasonal variability. They identified the Makran coast as a region with higher variability in significant wave height. Nevertheless, while the effects of monsoonal hydrodynamic changes on Makran coastal waves are of great importance for predicting the long-term performance of protective structures, most studies have targeted sediment transport (Bourget et al., 2010), climatic geomorphology (Kober et al., 2013), ecological risks (Kor et al., 2021), and cyclone hazards (Prizomwala et al., 2022; Haider et al., 2023).

Coastal waves can potentially pose substantial hazards such as shore erosion, inundations, property damage, and navigation hazards (e.g., Gao et al., 2021; Cao et al., 2022; Krishna et al., 2023; Uścinowicz et al., 2023). Considering significant energy in strongly forced wind-sea and long swell waves approaching the shorelines, coastal defense measures play a critical role. Amongst them, the construction of rubble mound breakwaters is widely recognized as the conventional approach for wave mitigation, offering advantages such as the ability to adapt to seabed alternations and shoreline variations and comparatively lower maintenance costs (Mahmoudof and Hajivalie, 2021; Li et al., 2022; Nguyen et al., 2022; Díaz-Carrasco, 2023). However, the mitigation of harbor oscillation, as a crucial problem challenging port operation, has been investigated in some recent studies (e.g., Wang et al., 2022; Dong et al., 2023; Gao et al., 2024). Assessing the hydraulic performance of existing harbor RMBs against seasonal variations of incoming waves is a hot topic in coastal engineering to determine whether the structures can meet their functional requirements (Galiatsatou et al., 2018; Sierra, 2019; Radfar et al., 2021). Therefore, an accurate understanding of RMBs interaction with nearshore processes, such as wave transformation (e.g., Harry et al., 2018; Mahmoudof et al., 2021c; Mahmoudof and Takami, 2022), breaking (e.g., W. Zhao et al., 2023), reflection (e.g., Díaz-Carrasco et al., 2021), and overtopping (e.g., Irías Mata and Van Gent, 2023), is very crucial. The challenges linked to the reflection of incoming waves off coastal structures and natural shorelines, however, are widely acknowledged as dangerous sea states from the point of view of vessel safety, port operability, sediment scour, and the performance of floating wave energy converter systems (Zanuttigh and Van der Meer, 2008; Barak et al., 2018; Zhang et al., 2020; Gao et al., 2023).

A majority of researchers agree that the Iribarren number or breaker parameter ξ is the most appropriate parameter for describing the waves interacting with coasts and structures (Battjes, 1974; Postma, 1989; Buccino and Calabrese, 2007; Iglesias et al., 2008; Myrhaug, 2020; Liu et al., 2021; Stagnitti et al., 2023):

$$\xi = \frac{\tan\alpha}{\sqrt{2\pi H_{m0}/gT_{p,o}^2}} \tag{1}$$

where $\tan(\alpha)$ is the structure or coast slope, H_{m0} denotes the significant wave height, $T_{p,o}$ is the offshore peak period, and g is the gravitational acceleration. However, the capability of ξ could be variable based on the spectral shape, the combination of the sea and swell waves, and their energy contents, or the intensity of wave breaking. Dekker et al. (2007) and Zanuttigh and Van der Meer (2008) emphasized replacing the peak period T_p with the spectral wave period T_{m-1} to reduce the variability of the reflection coefficient K_r with respect to ξ for shallow water situations or bimodal wave regimes. However, discussions regarding the optimal period parameter to minimize the scattering of predictions in nearshore areas are still in progress (e.g., Mahmoudof et al., 2023). Several spectral methods have been proposed to consider the effects of bimodal wave energy spectra, for example, geometric methods that use detected (two) peaks with a scale factor for wave run-up (Van der Meer, 1997). Nonetheless, more generic methods employ different orders of spectral moments of the wave energy spectrum to calculate spectral wave periods.

Utilizing negative-moment spectral periods has received much focus during the last two decades for describing wave run-up and overtopping over shallow foreshores (Hofland et al., 2017; Altomare et al., 2020; Liu et al., 2020; Mahmoudof et al., 2023). This is mainly because such spectral periods give more attention to lower frequencies in the wave energy spectrum than higher frequencies, which is more critical for shallow waters where infragravity waves and bimodal spectra appear (Zanuttigh and Van der Meer, 2008; Gao et al., 2018; Gao et al., 2019). Van Gent (2001) compared several characteristic periods (peak wave period T_p, mean wave periods T_{m1} and T_{m2}, and spectral periods T_{m-1} and T_{m-2}, see Section 3 for formulations) to evaluate the effects of wave energy spectra on wave run-up. He found that T_{m-1} brought out the lowest deviation between observations and computations; however, T_{m-2} resulted in only a 12% higher deviation compared to T_{m-1}. Van Gent (1999) reported that using T_{m-2} led to a 2.9% reduction in agreement between overtopping observations and calculations compared to T_{m-1}. Nevertheless, the capability of T_{m-2} to explain wave reflection off the coasts and structures remained unexplored in recent studies.

The first predictive formulas for the reflection coefficient K_r as a function of ξ were proposed in the 1970s (Bruun and Gunbak, 1976; Battjes, 1974; Losada and Giménez-Curto, 1980; Seelig and Ahrens, 1981; Postma, 1989; Van der Meer, 1992). Zanuttigh and Van der Meer (2008) and Zanuttigh et al. (2008) utilized a comprehensive database and performed an experimental investigation to establish a universal correlation for K_r calibrated for differ-

Table 1. Proposed equations for bulk reflection coefficient K_r. ξ is the breaker parameter, $tan(\alpha)$ is the structure gradient, P is the permeability factor (0.4 for multi-layered breakwaters), H_i is the incident wave height, L_0 is the offshore wavelength for the peak period, d_t is water depth at the structure toe, and D is the characteristic diameter of rock armours.

Authors	Proposed equations	Description
Battjes (1974)	$K_r = 0.1\xi^2$	
Losada and Giménez-Curto (1980)	$K_r = A(1-\exp(-B\xi))$	$A = 1.35$ and $B = 6.60$
Seelig and Ahrens (1981)	$K_r = \frac{A\xi^2}{\xi^2+B}$	$A = 0.60$ and $B = 6.60$
Postma (1989)	$K_r = 0.125\xi^{0.73}$	
Van der Meer (1992)	$K_r = 0.071P^{-0.082}(\tan\alpha)^{0.62}\left(\frac{H_i}{L_0}\right)$	
Davidson et al. (1996)	$K_r = 1.151\left(\frac{d_t L_0^2 \tan\alpha}{H_i D^2}\right)^{0.11}$	
Muttray et al. (2006)	$K_r = \frac{1}{1.3+3d_t\frac{2\pi}{L_0}}$	
Zanuttigh et al. (2008)	$K_r = \tanh(0.12\xi^{0.87})$	
Mahmoudof et al. (2021b)	$K_r = 0.16\xi^{0.70}$ and $K_r = \tanh(0.11\xi)$	

ent breakwater structures. They proposed a hyperbolic equation in terms of ξ with coefficients as functions of the roughness factor. Koutrouveli and Dimas (2020) found that the crest width does not notably affect the reflection coefficient; however, ξ and K_r are positively correlated. Through field observations, Mahmoudof et al. (2021b) investigated the bulk and frequency-dependent reflective response of a rubble mound breakwater and introduced a power-law equation for K_r. They indicated that prediction formulas utilizing the physical characteristics of the RMB are less accurate compared to those employing ξ parameter (see Figure 7 therein).

Nevertheless, physical features of porous structures were also examined to predict the reflection coefficient K_r, such as wave energy through permeable structures (Sollitt and Cross, 1972), toe depth (Seelig and Ahrens, 1981), shape and configuration of structures (Dattatri et al., 1978; Sulisz et al., 1989; Koutrouveli and Dimas, 2020), porosity (Kumar and Barak, 2007; Kumar et al., 2023), and armour size (Wilson and Cross, 1972; Requejo et al., 2002). Barak and Kaliraman (2019) demonstrated that the energy of transmitted and reflected waves from a porous structure depends on the angle of the incident waves. Some studies have also investigated the combined physical characteristics of RMBs and the hydrodynamics of incoming waves (Numata, 1976; Oumeraci and Partenscky, 1990; Van der Meer, 1992; Van der Meer and Daemen, 1994; Van der Meer et al., 2005; Peihong et al., 2021; Díaz-Carrasco et al., 2021; Díaz-Carrasco, 2023). Table 1 summarizes some available formulations for predicting K_r.

The literature review thus reflects significant efforts to understand the comprehensive impacts of monsoonal hydrodynamic changes in the Indian Ocean (e.g., Kober et al., 2013; Kor et al., 2021) in spite of a critical knowledge gap concerning their specific effects on the existing coastal structures' responses. Specifically, the seasonal variations in the reflective behavior of RMBs are remarkable, as these variations directly affect the RMB's functionality, navigability, and long-term structural integrity. In addition, several studies have used experimental setups to study wave reflection from RMBs either exclusively (Lee and Shin, 2014; Aniel-Quiroga et al., 2019; Salauddin and Pearson, 2020; Mostaghiman and Moghim, 2022) or alongside numerical models (Iglesias et al., 2008; Koley et al., 2020; Han et al., 2022). However, as far as the authors are aware, the works of Calhoun (1971), Davidson et al. (1996), and Mahmoudof et al. (2021b) are the only researches that utilized field measurements to propose reflection coefficient equations for RMBs. Given the scarcity of investigations into this precise aspect and the apparent lack of observations in real-life wave situations, our study endeavors to fill this void by comprehensively examining the seasonal variation of wave reflection off the structure. Through a one-year field measurement, this paper aims to evaluate the reflective performance of the RMB in the face of wave patterns driven by the Indian Ocean monsoon. To this end, seasonal variations of sea and swell waves' characteristics are investigated, focusing on the appropriate wave parameters and mathematical functions describing the reflection coefficients at the RMB of Chabahar Bay. However, the utilization of longer and more extensive datasets could enhance the accuracy of results and formulations in future research.

This paper is organized as follows. Section 2 provides an overview of the study area, focusing on wave and meteorological characteristics, measurement procedures, and structure specifications. Section 3 details the data processing methods employed in this research. Section 4 presents the research results. Discussion and concluding remarks are outlined in Section 5 and Section 6, respectively.

2. Study area

Chabahar Bay, situated at approximately 25.3019°N and 60.5962°E along the north of the Gulf of Oman, is an essential gateway for trade and connectivity in the southern part of Iran. The construction of Phase I of the Shahid-Beheshti breakwater began in 2003 and continued until 2012. Data collection for the current study was carried out when the primary breakwater was in place in 2006 and 2007. During that period, the seaward slope of the RMB had a gradient of 2:3, and its overall length spanned roughly 1,600 m. The breakwater components, including armour units, filter layers, and core materials, vary in size, with armour units weighing between 8 to 20 tons, filter layers ranging from 1 to 3 tons, and core layers less than 0.4 tons (Mahmoudof et al., 2021b; see Figure 2 therein for details). Considering the porosity of the studied breakwater and employing the formulations of Postma (1989), Van der Meer (1992), and Zanuttigh et al. (2008) yield comparable K_r values between ∼0.3 and ∼0.9 during winter monsoon (Mahmoudof et al., 2021b; see Figure 7 therein).

The study area experiences notable changes in its wave patterns due to seasonally reversing monsoonal winds. The shifting winds influence the climate in this area during the summer monsoon from May to August and the winter monsoon from November to February. The wind consistently blows from the southwest during the summer monsoon (Sanil Kumar et al., 2011; Radfar et al., 2021), while the winter monsoon brings northeasterly winds (Morrison et al., 1998; Aboobacker and Shanas, 2018). Several studies have examined the seasonal variations in the climatology of the Gulf of Oman. The distinct reversal patterns of wind associated with this region's winter and summer monsoons are respectively exemplified in Figures 6 and 7 of Chaichitehrani and Allahdadi (2018) as an example study. Consequently, the main factors driving waves in this area are twofold: the waves originated from equatorial latitudes and those from the Hormuz Strait in the eastern part of the Persian Gulf. The former generates more energetic waves, generally predominant in the summer monsoon. However, the latter produces moderate waves, particularly during the winter monsoon's extreme conditions.

Transitional or inter-monsoon periods are characterized by shifting wind patterns and weather conditions. During the pre-summer monsoon season, which typically takes place in March and April, northeast winds gradually shift to southwest winds; however, in the post-summer monsoon season, usually in September and October, the monsoon winds reverse from southwest to northeast (Düing, 1970; Vinod Kumar et al., 2014; Smith et al., 2020). It should be noted that the timing of transition periods can vary annually and may be seen at varying times across different geographical areas (Morrison et al., 1998; Samiksha et al., 2014; Z. Zhao et al., 2023). However, the summer monsoon, known by local natives as the 120-day winds due to the occurrence of strong winds, has a more distinct timing in the area. The wave system often combines the aforementioned patterns throughout the year, displaying bimodal wave energy spectra in different months (Saket and Etemad-Shahidi, 2012). The tidal regime in this region is meso-tidal, reaching a maximum range of around 2.7 m. The average highest high-water level stands at approximately 2.9 m, while the average lowest low-water level is about 0.8 m. The bathymetric map of the studied region, sourced from the Iranian National Cartographic Center in 2007, is depicted in Figure 1. This figure also denotes the precise locations of the breakwater and the measurement station.

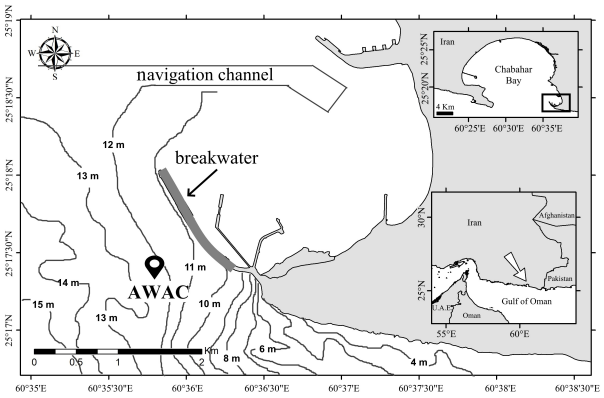

Figure 1. The bathymetric map of the surveyed region (sourced from the Iranian National Cartographic Center, 2007), highlighting the placement of the breakwater as well as the AWAC installation (Mahmoudof et al., 2021b).

The study area features a rocky seabed, making it suitable for placing the bed-mounted instruments and accessories. Therefore, a Nortek AWAC wave recorder was fixed to the bed to collect directional wave data at a sampling frequency of 2 Hz. It was installed in the west-southwest of the studied RMB, approximately 750 m away at coordinates 25.2896°N and 60.5945°E, as indicated in Figure 1. Data collection spanned from September 1, 2006, to August 31, 2007. The directional wave data was recorded in 17.07-minute bursts each hour. Throughout this measurement period, a total of 7228 time series were successfully recorded. However, a RAM malfunction disrupted the sequence of consecutive bursts during October 2006, resulting in a one-month data gap within the measurements.

In the study area, as shown in Figure 1, the water depth typically varies from 5 to 13 m. The water depths at the RMB toe and the measurement station were approximately 11.6 and 12.5 m, respectively. The seabed between the breakwater and the AWAC location is generally even and gradually sloped, featuring depths ranging from 11 to 13 m, except for a short segment of the breakwater's southeastern part that has minimal impact on wave transformation patterns. Consequently, only slight changes in wave heights due to shoaling and de-shoaling of incident and

reflected waves were anticipated, with negligible changes in reflected wave intensity due to refraction and dispersion effects. Additionally, significant attention was given to ensuring the reliability of measurements regarding the diffraction of reflected waves at the measurement station. Using spectral characteristics of waves and dimensional specification of the RMB on the diffraction charts provided by Goda (2010), it was determined that the diffraction coefficient of reflected irregular waves at the AWAC position is unity. It means that the diffraction effect of reflected waves is negligible, indicating that the characteristics of the incident and reflected waves at the instrument location are nearly identical to those at the structure's toe. Furthermore, any potential alterations in the shoaling or refraction of incidence waves could be primarily counterbalanced by the de-shoaling and opposing refraction of reflected waves.

3. Data processing and methods

This investigation employed directional wave data from a Nortek AWAC wave recorder to deduce the wave reflection coefficients. The AWAC applies Acoustic Surface Tracking (AST) and Particle Velocity (PV) techniques to record the directional distribution of wave energy. Most bottom-mounted directional-wave measurement instruments like AWAC use the acoustic Doppler technique. However, instruments utilizing only the combined pressure-velocity (PUV) approach are limited to the depth of installation due to the attenuation of the surface signals. AWAC equipped with AST and PUV is even capable of measuring waves with a period smaller than 2 s and amplitude smaller than 5 cm when deployed at depths as deep as 60 m (Pedersen and Lohrmann, 2004). The AST can sample at a rate as high as 4 Hz. Pedersen et al. (2007) showed that more than 99% of all AST measurements successfully passed the quality control checks. Additionally, measurements of wave height and period showed excellent agreement with the data collected by the surface wave buoy. Observations of this study do not clearly fall within the instrumental limitations of AWAC (Figures 9–11).

The initial analysis of the AWAC measurements was carried out using the STORM software, enhancing the computation of directional wave energy spectra using the Maximum Likelihood Method for Surface Tracking (MLMST). Directional spectra $e(f,\theta)$ are obtained by merging one-dimensional energy spectra $E(f)$ and directional spreading $D(f,\theta)$, as outlined below:

$$e(f,\theta) = E(f)\,D(f,\theta) \tag{2}$$

In order to exclude the impact of infragravity and capillary waves, a frequency band between 0.04 and 0.30 Hz was chosen for wind wave analysis (Mahmoudof et al., 2021a). The significant spectral wave height (H_{m0}) was

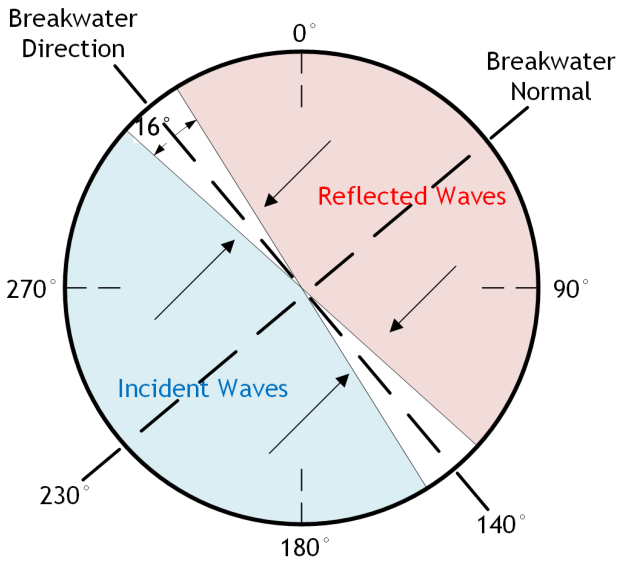

Figure 2. Breakwater direction, normal direction, incident, and reflected waves in the nautical system (Mahmoudof et al., 2021b).

determined through the energy density distribution within this frequency range. A frequency threshold of 0.125 Hz was applied to distinguish between sea and swell waves. Figure 2 shows the semi-circle divisions separating the energy density of incident and reflected waves. In this specified directional arrangement, any incoming wave falling within the incomplete semi-circle of incident waves $(148^\circ < \theta < 312^\circ)$ is subsequently reflected in the segmented range of reflected waves $(328^\circ$ or $-32^\circ < \theta < 132^\circ)$ in the nautical system, as illustrated in Figure 2. Two directional sectors spanning 8° were omitted from the beginning and end sections of both incident and reflected ranges, a measure taken to account for potential compass inaccuracies. It should be noted that the normal components of the incident and reflected waves' energy with respect to the breakwater direction were taken into account to calculate the reflection coefficient, ignoring the energy of waves along the RMB. Considering the extremely short fetch available for local northern wind in Chabahar Bay, reflected waves are not contaminated by northern sea waves (Mahmoudof and Azizpour, 2020; Mahmoudof et al., 2021a). The predefined frequency threshold of sea-swell waves (0.125 Hz) was applied in the semi-circle of incident waves (148°–312°) to calculate the average incident directions of sea and swell waves separately.

The directional spectra encompassed energy distribution across 90 directions $(\Delta\theta = 4^\circ)$ and 198 frequency bands $(\Delta f = 0.01\,\text{Hz})$. Consequently, following Lykke Andersen and Burcharth (2009), the energy of incident $(E_{inc,p})$ and reflected $(E_{ref,p})$ waves, both in the direc-

tion perpendicular to the breakwater, were calculated as follows:

$$E_{\text{inc, p}} = \int_{f=0.04}^{0.30} \int_{\theta=148}^{312} e(f,\theta) \cos\beta d\theta df \tag{3}$$

$$E_{\text{ref, p}} = \int_{f=0.04}^{0.30} \int_{\theta=328}^{132} e(f,\theta) \cos\beta' d\theta df \tag{4}$$

where β and β' represent the angles between breakwater normal and the incident and reflected directional wave energy, respectively. Consequently, the significant wave heights of incoming sea and swell waves were obtained by:

$$H_{m0,\text{swell}} = 4 \times \sqrt{\int_{0.040\,\text{Hz}}^{0.125\,\text{Hz}} e_{\text{inc}}(f)\, df}, \tag{5}$$

$$H_{m0,\text{sea}} = 4 \times \sqrt{\int_{0.125\,\text{Hz}}^{0.300\,\text{Hz}} e_{\text{inc}}(f)\, df} \tag{6}$$

where $e_{\text{inc}}(f)$ is the spectral energy density of incident waves. For each data burst, bulk-averaged wave reflection coefficient K_r was calculated using Eqs. (3) and (4) as:

$$K_r = \sqrt{\frac{E_{\text{ref, p}}}{E_{\text{inc, p}}}} \tag{7}$$

To weigh different wave frequencies within the bimodal energy spectrum, Iribbaren number ξ was calculated using several spectral periods – peak wave period T_p (as the significant period of wave energy spectrum), mean periods $T_{m1} = m_0/m_1$ and $T_{m2} = (m_0/m_2)^{0.5}$, and negative-moment spectral periods $T_{m-1} = m_{-1}/m_0$ and $T_{m-2} = (m_{-2}/m_0)^{0.5}$, where the n^{th} spectral momentum of the wave energy spectral density $E(f)$ is $m_n = \int_0^\infty f^n E(f) df$. The optimal characteristic wave period parameter leaves the lowest spreading around the prediction fit for each month. Therefore, the coefficient of determination R^2 was used as a statistical measure to compare the influence of different wave periods. In addition, statistical hypothesis tests and Analysis of Variance (ANOVA) for a significance level of 0.05 are used to assess the overall statistical significance of a regression model and to compare the statistical difference between the coefficients of two regression models over a single observation data. The probability values associated with these hypothetical tests (p-value) are compared with the significance level of 5% to determine the level of statistical significance in the hypothesis tests.

4. Results

4.1 Characteristic period parameter

As mentioned above, most studies have introduced the Iribarren number as a function of wave period as the best parameter describing the wave interactions with coasts and structures. Figure 3 shows four examples of the variations of wave reflection coefficient K_r against the Iribarren number ξ_p, in which the subscript p indicates that ξ is calculated using the spectral peak period T_p. The observations presented in this figure are associated with pre-summer and post-summer monsoon months characterized by wave regimes composed of sea and swell waves, which exhibit a continuous (but non-uniform) energy distribution across a broad frequency range. The figure shows that using T_p leads to separating data clouds into two or more groups and highlights an apparent lack of correlation between ξ_p and K_r. The primary cause for the discrepancy when using T_p is that the frequency distribution of energy is no longer considered, and thus, the spectral shape and energy weighting within the spectrum have no effect on ξ_p.

A similar pattern of separation (not shown here) was observed in almost all months when the spectral mean periods T_{m1} and T_{m2} were employed; more specifically, using T_{m2} created more disconnected and discordant results than T_{m1}. The increasing deterioration by using higher positive-moment spectral periods was also confirmed by Van Gent (1999) for run-up and overtopping observations. More consistent results might be yielded utilizing negative-moment spectral periods T_{m-1} and T_{m-2}, including more attention to the energy of low-frequency waves. Although not shown here, an analogous analysis was also performed to produce the results for Iribarren numbers calculated by T_{m-1}. Finally, Figure 4 shows the monthly results of wave reflection as a function of T_{m-2}, referred to as ξ_{m-2}. Following several studies in which a power-law equation is used to predict wave reflection coefficient as a function of ξ (see Table 1), the best-fit power laws $K_r = a\xi^b$ over monthly wave data are also shown. Since previous studies have proposed different reflection coefficient equations in terms of ξ parameter, the prediction performance of these equations is examined on the present dataset in Appendix A. Besides, prediction formulae considering the physical characteristics of RMB are shown to be less efficient than those by ξ parameter for the observations considered here (Mahmoudof et al., 2021b; see Figure 7 therein). Therefore, new fits are proposed here (see Sections 4.2 and 4.3), predicting the reflection coefficient based on the ξ parameter as the primary indicator for the hydrodynamic characteristics of the incident waves. The performance of these new predictions is also compared with preexisting formulae in Appendix A.

In Figure 4, sea-dominated waves (waves with sea energy larger than 50%) and swell-dominated waves (waves with swell energy larger than 50%) are deliberately presented in different colors to show that sea-dominated waves

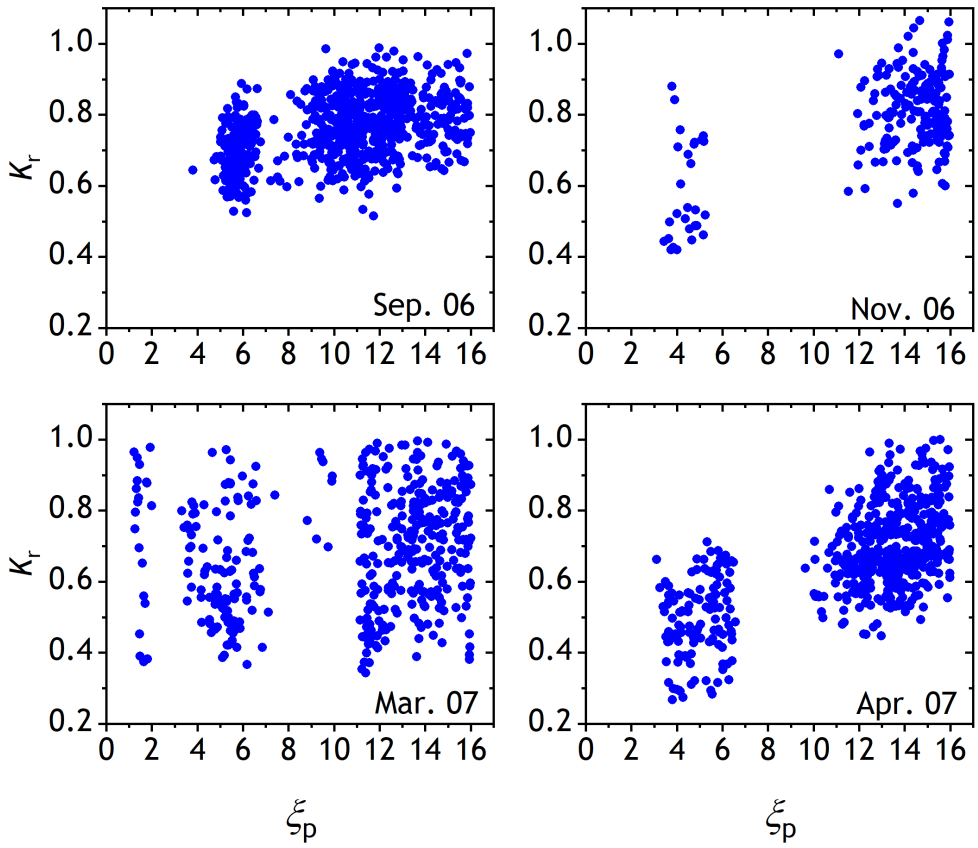

Figure 3. Separated observations of K_r against Iribarren number ξ_p calculated by peak period T_p.

Table 2. The values of R^2 for power laws fitted over monthly reflection coefficient measurements using T_{m-1} and T_{m-2}. Differences in R^2 are obtained relative to T_{m-1}.

Month	Coefficient of determination R^2		Difference (%)
	T_{m-1}	T_{m-2}	
Sept. 2006	0.36	0.34	−5.56
Nov. 2006	0.54	0.57	5.56
Dec. 2006	0.67	0.73	8.96
Jan. 2007	0.41	0.51	24.39
Feb. 2007	0.62	0.69	11.29
Mar. 2007	0.78	0.80	2.56
Apr. 2007	0.69	0.72	4.35
May 2007	0.44	0.42	−4.55

frequently attain lower values of ξ_{m-2} and K_r. In this figure, the curves have been fitted to monthly data and extended for ξ_{m-2} values between ~ 2 and ~ 16 to facilitate comparison. The K_r values obtained for February 2007 range from approximately 0.25 to 0.9, aligning with those calculated using the formulations of Postma (1989), Van der Meer (1992), and Zanuttigh et al. (2008), as reported in Mahmoudof et al. (2021b). Table 2 summarizes R^2 values for the power laws fitted over K_r values using T_{m-1} and T_{m-2}. It is shown that using T_{m-2} can enhance the prediction accuracy by up to 24% for meaningful values of R^2; however, the larger R^2 values are concurrent with the winter monsoon, when reduced scattering can be seen in observations.

Figure 4 proves that the reflection coefficient for swell-dominant waves is frequently higher than that for sea-dominant waves. The intense breaking of sea waves due to higher wave steepness leads to reduced reflection coefficient values compared to swell waves. Conversely, since swell waves break moderately, they boost the energy levels of seaward waves, leading to elevated wave reflection coefficients. This can be understood from the energy balance equation $K_r^2 + K_t^2 + K_d^2 = 1$, where K_d and K_t are wave energy dissipation and transmission coefficients, respectively (see, e.g., Van Gent et al., 2023). This general trend was accurately examined by Mahmoudof et al. (2021b) through frequency-dependent analysis of wave reflection for the same data set. They found that the increase in reflected waves' energy at both high and low frequencies during dominant swell periods can be understood as a consequence of energy transfer from the peak frequency to lower and higher harmonics, as reported previously by Masselink (1998). This transfer occurs due to the moderate breaking of long swell waves. On the other hand, during locally generated storms, the intense breaking of short sea waves leads to energy dissipation for most frequencies, especially the higher harmonics (see Figure 14

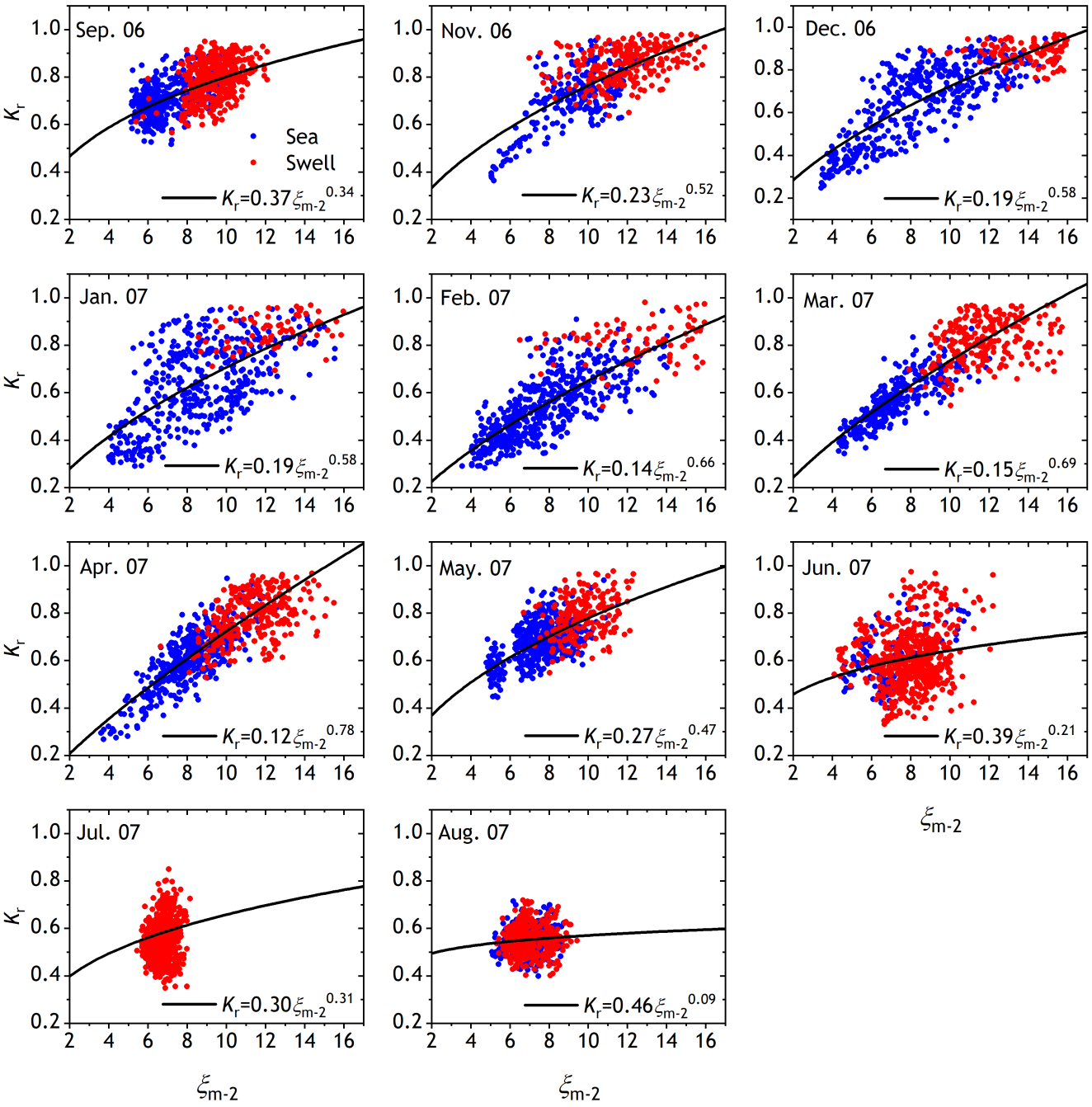

Figure 4. Monthly variations of reflection coefficient K_r of sea-dominated (blue dots) and swell-dominated waves (red dots) against Iribarren number ξ_{m-2}. The black line is the fitted power law on the overall waves (sea- and swell-dominated waves), the equation of which is written in each panel.

in Mahmoudof et al., 2021b). These frequency-dependent processes lead to higher and lower values of bulk reflection coefficient for wind-swell and sea-dominant waves, respectively. However, relatively lower reflection coefficient values for swell-dominant waves observed during summer monsoon (May, June, July, and August) is due to increased wave steepness as a result of more growth of wave height than wavelength.

4.2 Winter monsoon pattern of the reflection coefficient

It is evident from Figure 4 that it is not statistically possible to determine a consistent agreement and identify a global trend for changes in reflection coefficients throughout the entire year. This is mainly due to the monsoonal character of atmospheric circulation, different wave generation sources, multimodal spectral peaks, and varying sea-swell

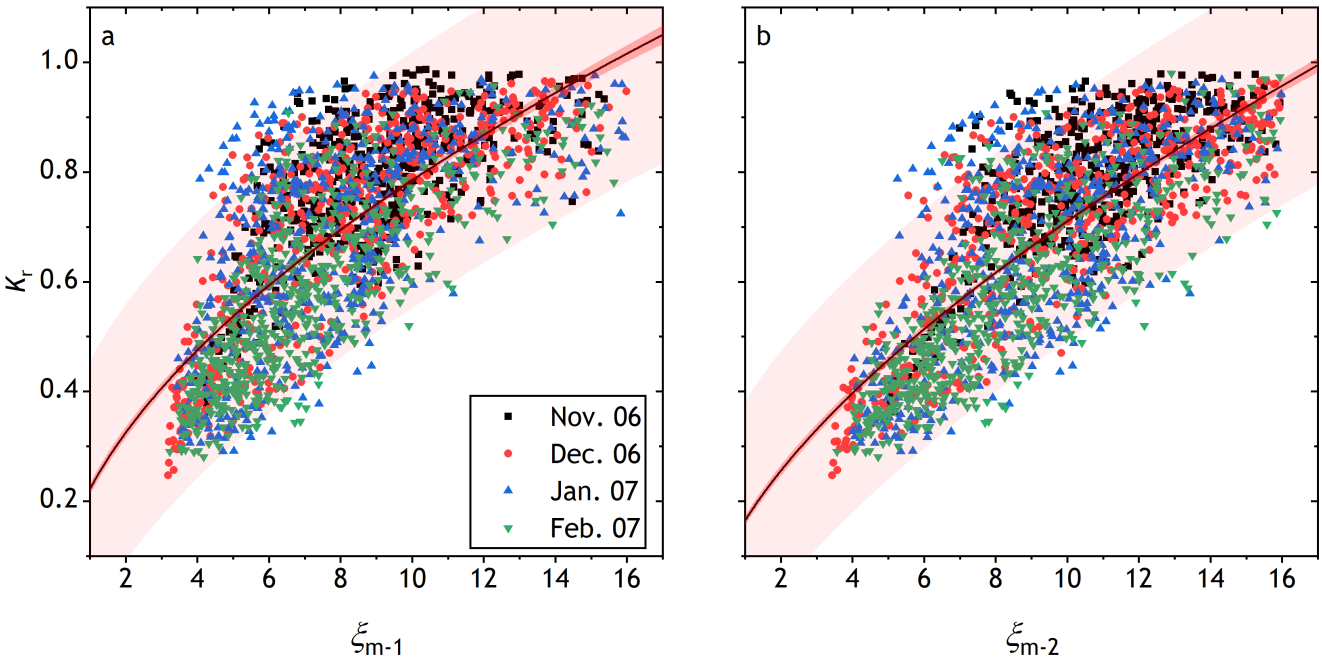

Figure 5. Scatter plots of reflection coefficient K_r for winter-monsoon seasons against Iribarren number ξ_{m-1} (panel a) and ξ_{m-2} (panel b). Fitted power-law equations are Eq. (8) (panel a) and Eq. (9) (panel b), along with 95% confidence bands (narrow-shaded regions) and prediction bands (wide-shaded regions).

waves combination from different directions in the region (Sanil Kumar et al., 2011; Aboobacker and Shanas, 2018; Anoop et al., 2020). In fact, the monthly variations in hydrodynamic characteristics and energy content of incoming waves induced by such monsoonal changes alter the structural response in a way that renders the annual bulk prediction model ineffective. However, by comparing the monthly variations of wave reflection measurements in Figure 4, one can categorize the reflection behavior of the RMB in terms of time into three categories: summer monsoon (May to August), winter monsoon (November to February), and transitional seasons (March, April, September, and October). It is worthwhile to emphasize again that this classification may vary annually; however, it is favored for studying marine meteorology in the investigated region (Morrison et al., 1998; Samiksha et al., 2014; Anoop et al., 2020).

Pairwise Analysis of Variance (ANOVA) at the significance level of 0.05 showed that the coefficient and exponent of fitting power law over each winter-monsoon month are significantly different from those of other months (p-value = 0.00). This discrepancy primarily arose due to variations in the characteristics of incoming waves resulting from differing wind sources each month. However, as shown in Figure 5a statistical analysis demonstrates that a global power law could be fitted over all winter-monsoon observations with $R^2 = 0.56$, given by:

$$K_r = (0.18 \pm 0.01)\,\xi_{m-1}^{(0.64\pm0.01)} \tag{8}$$

ANOVA analysis on the coefficient and exponent of Eq. (8) shows that they significantly differ from zero (p-value = 0.00). The same analysis for observations normalized by ξ_{m-2} was also performed, which is shown in Figure 5b. The global fitting for such observation resulted in a power law with $R^2 = 0.65$, as follows:

$$K_r = (0.14 \pm 0.00)\,\xi_{m-2}^{(0.71\pm0.01)} \tag{9}$$

An ANOVA analysis was also conducted to verify the statistical differences between Eqs. (8) and (9). The results indicated that the p-value associated with the hypothesis suggesting similarity between the two regression models was zero. This evidence points to the conclusion that ξ_{m-2} offers an almost noticeable improvement in the prediction of reflection coefficients, exhibiting an approximate 16% enhancement in R^2 values compared to the ξ_{m-1} formulation. This marked increase in R^2 values highlights the superiority of T_{m-2} as a characteristic period parameter to more accurately describe the observed data during winter-monsoon months.

4.3 Summer monsoon pattern of the reflection coefficient

Concerning the summer monsoon phenomenon, it is worth noting that there were again notable statistical disparities observed when comparing monthly data with each other. Furthermore, a comprehensive global fitting analysis was carried out to investigate the reflective behavior of the RMB

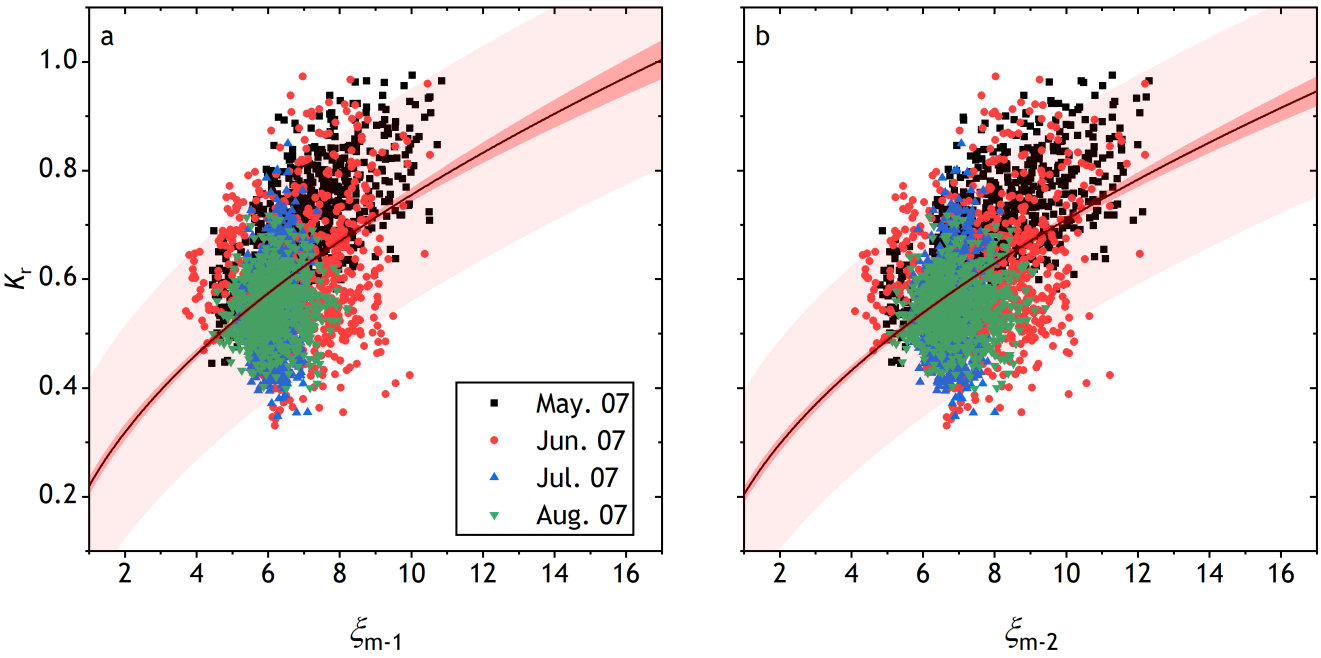

Figure 6. Same as Figure 5 but for the summer monsoon seasons as predicted by Eq. (10) (panel a) and Eq. (11) (panel b).

during the summer monsoon, and the results indicated significant statistical distinctions between observations formulated using ξ_{m-1} and those derived from ξ_{m-2}. For the case of ξ_{m-1}, the outcomes are visually represented in Figure 6a with R^2 value of 0.20, given by:

$$K_r = (0.22 \pm 0.01)\,\xi_{m-1}^{(0.54\pm0.02)} \tag{10}$$

However, upon closer examination of the ξ_{m-2} formulation, the fitting results are illustrated in Figure 6b, accompanied by an R^2 value of 0.23, which is determined as follows:

$$K_r = (0.20 \pm 0.01)\,\xi_{m-2}^{(0.54\pm0.02)} \tag{11}$$

An ANOVA analysis was also conducted to assess the statistical distinctions Eqs. (10) and (11). The outcome of this analysis indicated the p-value $= 0$, leading to the conclusion that ξ_{m-2} offers a partially improved fit to the observed data compared to ξ_{m-1}, demonstrating an approximate 15% improvement in R^2 values compared to the ξ_{m-1} formulation. Although statistical analysis reveals that the fitted functions are indeed different from each other, from an engineering viewpoint, these two functions fail to exhibit significant practical distinctions. Therefore, considering the small values of R^2, it can be stated that substituting T_{m-2} for T_{m-1} results in a trivial improvement in predicting wave reflection coefficients for engineering applications.

Here, it should be mentioned that the prediction of K_r for the entire one-year dataset is provided in Appendix A, leading to $K_r = 0.17\xi_{m-2}^{0.63}$ with $R^2 = 0.51$. The bulk data analysis indicates that the derived equation does not show a significant difference compared to some previously suggested equations (see Figure A1 in Appendix A), confirming that the physical and dimensional conditions of the RMB remained unchanged throughout the one-year study period. However, such an equation cannot capture the different dependencies of the reflection coefficient on the Iribarren number in winter and summer monsoon periods (as indicated by varying R^2 values in Eqs. (8)–(11)). Furthermore, it has been demonstrated that the proposed equation in this study predicts the bulk dataset with higher accuracy compared to those suggested previously (see Table A1 in Appendix A). The evaluation of the previously proposed equations against the present monsoonal observations (see Figure A2 in Appendix A) also yields that Eqs. (8)–(11) provide more accurate predictions compared to the previous studies (see Figure A2 and Table A1 in Appendix A). Additionally, the previous predictions provide higher accuracy using ξ_{m-2} compared to ξ_{m-1}, although this increase in accuracy is more significant for winter monsoons than summer monsoons. The reasons for such differences between monsoonal seasons are explained in detail in Section 5.

4.4 Hyperbolic tangent prediction formulation

Regarding the form of mathematical equation that best fits the variations of K_r against ξ, most researchers have favored power law, as can be understood from Table 1. Mahmoudof et al. (2021b) conducted a statistical analysis aimed at determining the most suitable mathematical func-

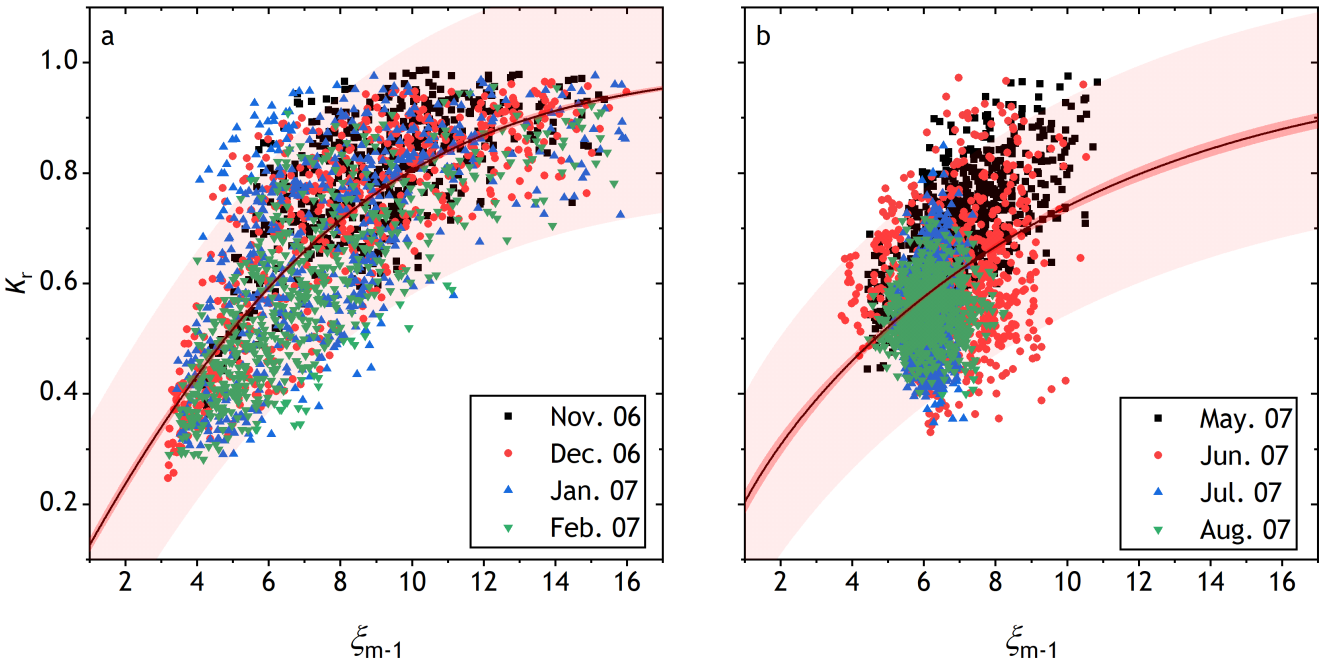

Figure 7. Scatter plots of reflection coefficient K_r against Iribarren number ξ_{m-1} during winter-monsoon seasons (panel a) and summer monsoon seasons (panel b). Fitted hyperbolic laws are Eq. (13) (panel a) and Eq. (14) (panel b), along with 95% confidence bands (narrow-shaded regions) and prediction bands (wide-shaded regions).

tion for approximating the best fit to the variations of K_r as a function of ξ_{m-1} for a field data set. Four mathematical functions – exponential, linear, logarithmic, and power law – were evaluated for this purpose, highlighting the power-law equation as the most accurate choice. Nevertheless, one drawback of power laws is the lack of control over their upper bounds for high values of ξ, potentially resulting in reflection coefficients exceeding the unity. Mahmoudof et al. (2021b) calibrated the following hyperbolic function to rectify the performance of their power-law prediction (see Table 1) at high ξ values:

$$K_r = (\tanh(a\xi))^b \tag{12}$$

with $a = 0.11$ and $b = 1.00$ for their specific data set. One advantage of Eq. (12) is that it approaches one asymptotically for high values of ξ. In this study, Eq. (12) was fitted over monthly observation, leading to satisfying overall fit statistics, though not shown here. However, this formulation was used for monsoon-categorized data normalized by T_{m-1} and T_{m-2}. The results for winter-monsoon observations are presented in Figure 7a in terms of ξ_{m-1}, with a hyperbolic fit with $R^2 = 0.59$ given by:

$$K_r = (\tanh(0.11\xi_{m-1}))^{0.93} \tag{13}$$

In a similar way, the results of the wave reflection coefficient during summer monsoon months employing T_{m-1} as the scaling parameter are shown in Figure 7b. The overall best fit can be expressed by:

$$K_r = (\tanh(0.07\xi_{m-1}))^{0.60} \tag{14}$$

with $R^2 = 0.20$. Regarding the ξ_{m-2} formulation, Figure 8a illustrates K_r observations during the winter-monsoon seasons, along with the corresponding fitted hyperbolic function with $R^2 = 0.64$ in the form:

$$K_r = (\tanh(0.10\xi_{m-2}))^{1.04} \tag{15}$$

However, using ξ_{m-2} to predict summer monsoonal variations of K_r leads to the following hyperbolic expression with $R^2 = 0.22$, as shown in Figure 8b:

$$K_r = (\tanh(0.06\xi_{m-2}))^{0.60} \tag{16}$$

By comparing Eqs. (14) and (16), it can be deduced that similar to power-law functions, using T_{m-2} in the hyperbolic functions does not substantially improve the accuracy of predicting the reflection coefficient during the summer monsoon. Nonetheless, a comparison between Eqs. (13) and (15) reveals a significant improvement in R^2 values from 0.59 to 0.64. Such substantial enhancement provides a valid rationale for using T_{m-2} during the winter monsoon period in coastal engineering applications.

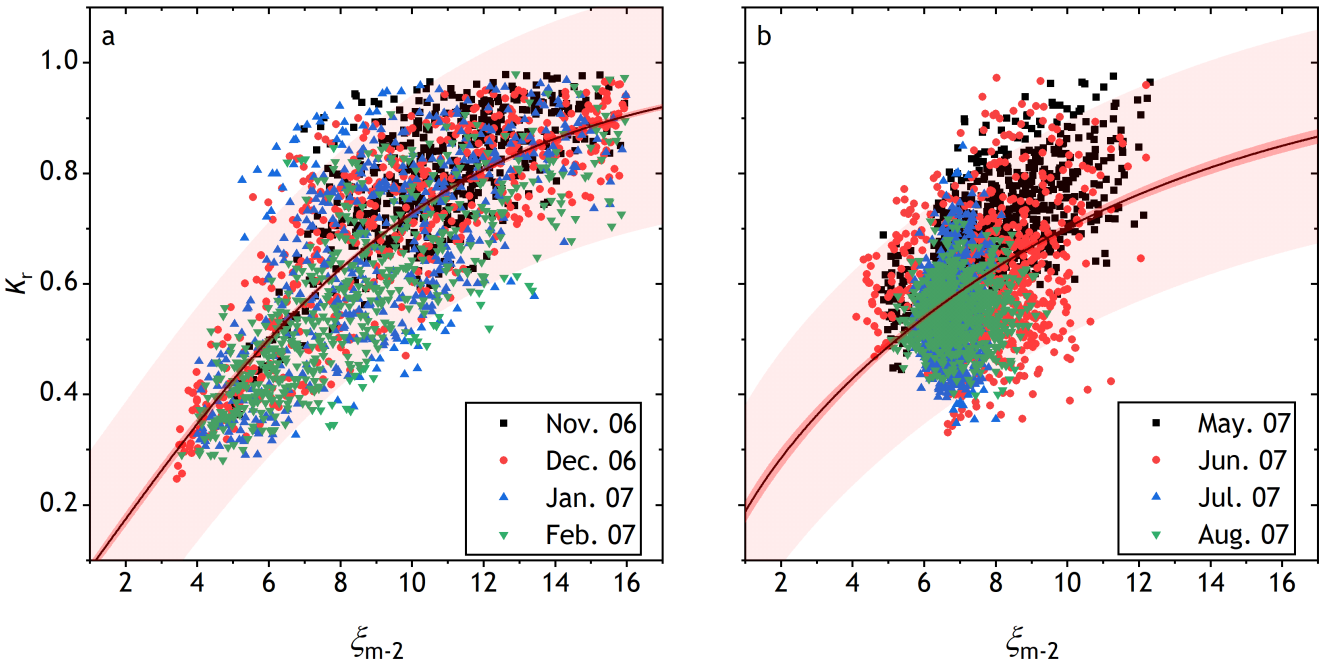

Figure 8. Same as Figure 7, but for ξ_{m-2} as predicted by Eq. (15) (panel a) and Eq. (16) (panel b).

5. Discussion

In the previous section, the reflective response of the RMB during observational months was quantitatively analyzed, leading to deriving different reflection prediction equations in the course of summer and winter monsoons. Nevertheless, one question remained undisclosed: what is the underlying reason for the significant difference in ξ and K_r values and their associated scattering during the summer and winter monsoons?

Figure 9 demonstrates that during the winter-monsoon months (November, December, January, and February), the wave field is a combination of moderate sea waves with heights frequently between 0.5 and 1 m and weak swell waves with heights less than 0.25 m. The effects of shallow bathymetry and very limited fetch length (Eyhavand-Koohzadi and Badiei, 2021, 2022) control the growth of sea waves associated with winter-monsoonal northeasterly winds (e.g., Neelamani et al., 2007; Kamphuis, 2010; Li et al., 2020). In addition, the mean directions of waves approaching the location of observations are provided in Figure 10, highlighting different generation sources of sea and swell waves. Consequently, the wave spectra mainly consist of two distinct sources with different incident directions and distinct peaks attributed to sea and swell waves, as shown in Figure 10. Considering such a wave field, the shorter wavelength of the sea waves and the longer wavelength of the swell waves contribute to forming a wide range of ξ values between $\sim$2 to $\sim$16. This is mainly due to the wavelength affecting more significantly on the reflection than the wave height (Postma, 1989; Díaz-Carrasco et al., 2021). Furthermore, considering the discussion on the range of K_r values for sea and swell waves (Section 4.1), the range of the reflection coefficient during winter-monsoon seasons has also increased, leading to a quite narrow distribution of K_r against ξ and the reduction of scattering in the observations.

Moving on towards the transitional pre-summer monsoon months of March and April and shifting in wind direction to the southwest, ξ and the K_r values are observed to fluctuate in almost less scattering (Table 2). However, the wave field is still combined with the sea and swell waves from different directions (see Figure 10). Almost similar incident wave field during pre-summer monsoon seasons relative to winter-monsoon conditions, and hence similar wave breaking on the RMB and reflected wave heights creates the close performance of the structure in these monsoonal seasons.

With the dominance of summer monsoon southwesterly winds from May to August, the persistent presence of highly energetic long-period waves characterized by very peaked wave energy spectra was observed (Figure 11) due to stronger wind relative to the winter monsoon period (Morrison et al., 1998; Aboobacker and Shanas, 2018; Anoop et al., 2020). Despite the dominance of high-energy swell waves with considerably growing heights originating from the strong southwest monsoon winds (Vinod Kumar et al., 2014; Anoop et al., 2020), the spectral period changes insignificantly (Aboobacker et al., 2011; Sanil Kumar et al., 2011). This leads to an escalation in the steepness of the long-period waves and slight reduction of ξ values from the range of 4–16 during the winter monsoon to approximately 4–10 during the summer monsoon (Figure 4). In

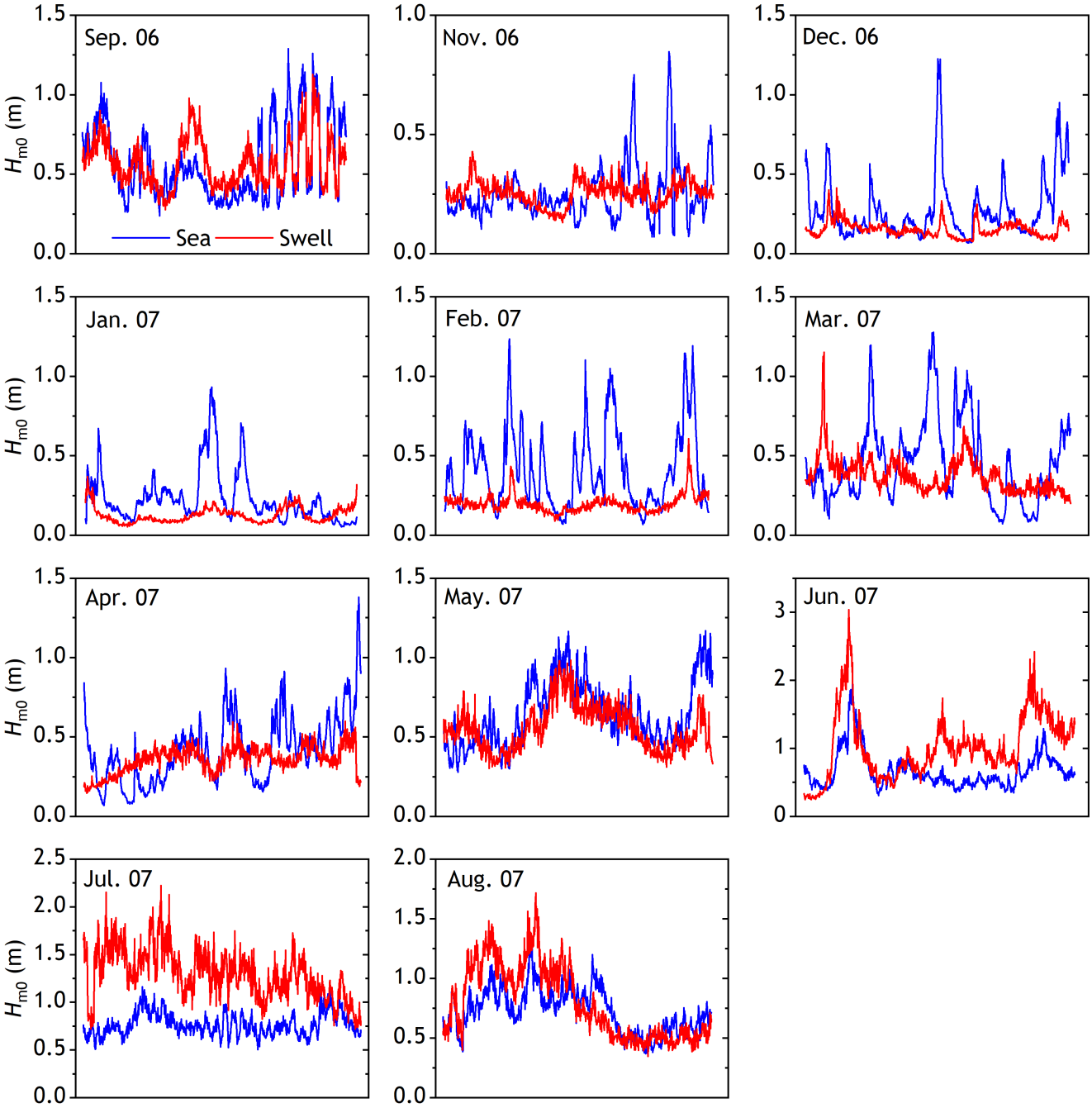

Figure 9. Time series of monthly observations of significant wave height H_{m0} for sea (blue line) and swell (red line) waves. The time axis is extremely compressed; therefore, it is left unmarked.

addition, the reduction of K_r could be attributed to the increasing wave steepness (e.g., Nassar et al., 2018; Pratola et al., 2021) and their almost severe breaking (Andersen, 2006; Zanuttigh and Van der Meer, 2008). Van Gent et al. (2023) explained that flow towards wave direction through permeable RMBs might be responsible for reducing K_r values. However, the presence of bubbles and spray of water particles up to a height of $\sim$15 m in the region provide further evidence for the intense breaking of swell waves and possibly energy transfer into alongshore flow and air. Therefore, decreasing K_r and ξ values and energy dissipation due to intense wave breaking give rise to a considerable spreading and scattering in the reflective response of the RMB around the general $K_r - \xi$ fit in the course of summer monsoon period.

During the post-summer monsoon months of September and October – the data for October was missed due to system error – a combination of sea and swell waves

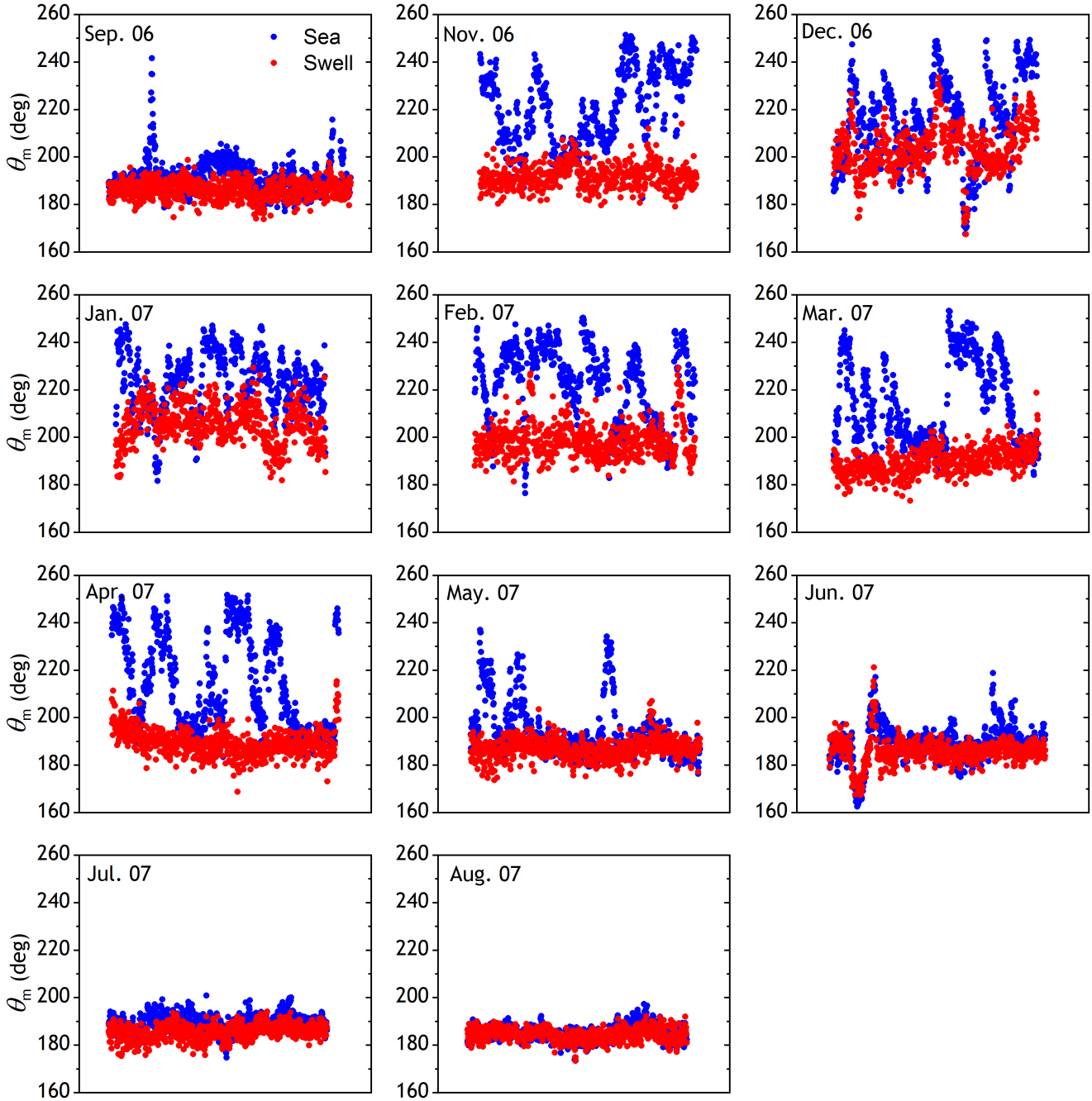

Figure 10. Time series of monthly observations of the mean direction θ_m for sea (blue dots) and swell (red dots) waves. The time axis is extremely compressed; therefore, it is left unmarked.

with moderate energy content is observed. In addition, the difference between the incoming direction of sea and swell waves is relatively more pronounced compared with the summer monsoon months (Figure 10) but not as distinct as the winter monsoon. This can be justified by a combination of unimodal and bimodal wave energy spectra, as shown in Figure 11. In other words, the wave field tends to transfer from the unimodal regime of summer monsoon into the bimodal regime of winter monsoon.

Figure 10 also justifies the improvement in the R^2 values presented in Table 2. During the winter-monsoon and pre-summer monsoon months characterized by sea and swell waves with different incident directions and double-peak wave energy spectra, using T_{m-2} leads to an enhancement in predicting the reflective behavior of the structure and reduces the scattering of observations. However, during the summer monsoon with sea and swell waves with equal incident directions and single-peak wave energy

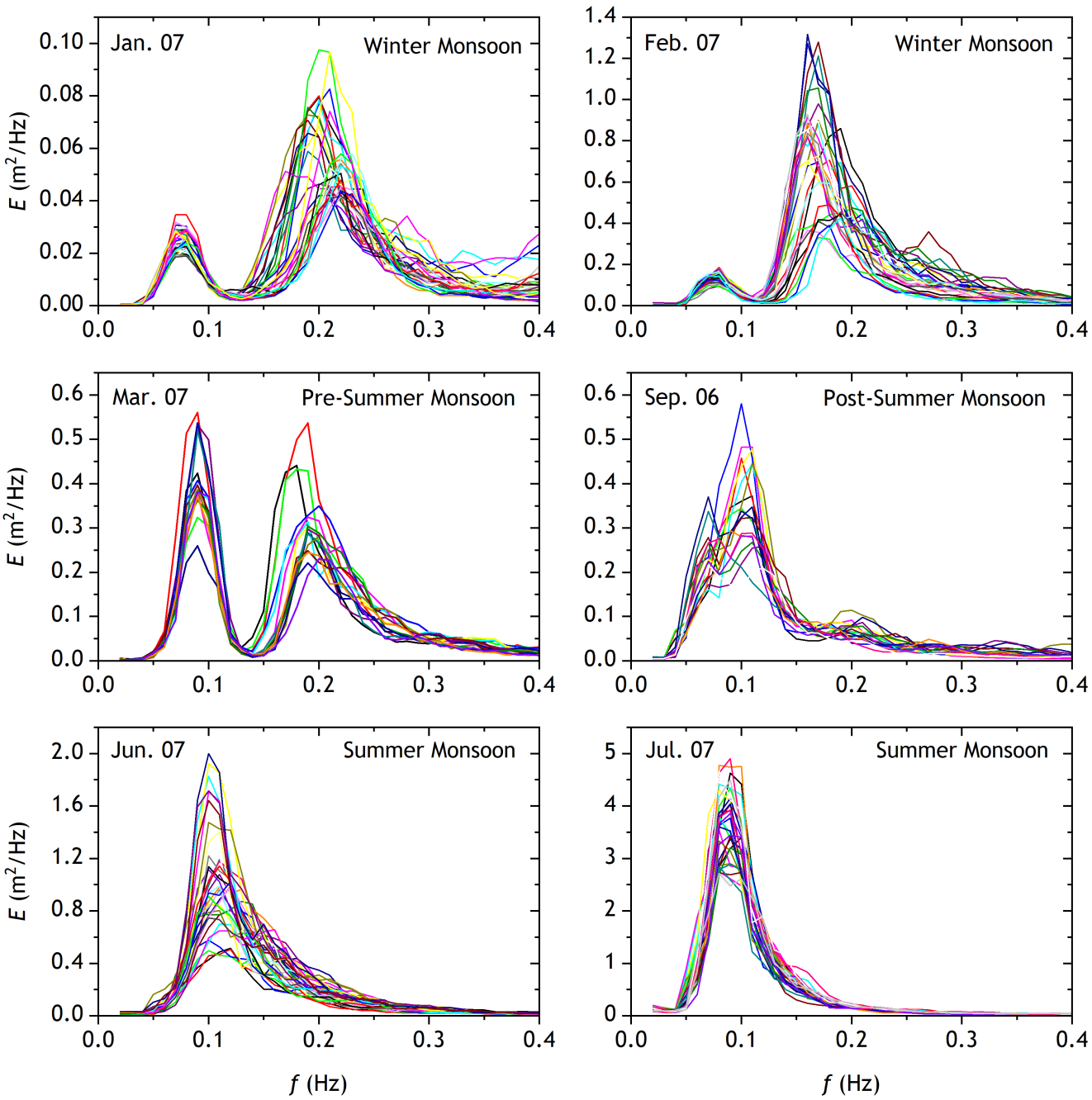

Figure 11. Representative spectra of observation during winter-monsoon months (top panels), inter-monsoon months (middle panels), and summer monsoon months (bottom panels).

spectra, utilizing T_{m-2} does not create a significant difference in the mentioned behavior. However, using the peak wave period in predictions on wave reflection coefficient for all monsoonal periods may lead to significant inaccuracies (see Figure 3), as suggested by, for example, Van Gent (1999, 2001) and Stagnitti et al. (2023) for wave run-up and overtopping phenomena.

To sum up, seasonally varying reflective responses of the RMB depends on several factors. During the winter monsoon, different incoming directions of incident waves and moderate energy content of the sea-swell wave field give rise to bimodal spectra across a wide frequency range. Such multimodal spectrum forms a diverse range of wavelength values (and consequently ξ values). Due to their low steepness, such waves do not break much; hence, most of them are reflected by the RMB. Therefore, the reflective behavior of the RMB in the winter monsoon depends more on ξ, or is generally more predictable.

However, in the summer monsoon, incident waves predominantly come from one direction and carry substantial energy. Consequently, various breaking processes dissipate a significant portion of this energy. On the one hand, this leads to a reduction in the reflection coefficient, and and as a result, it diminishes the dependency of the reflection coefficient on ξ. These influential characteristics of incident waves (such as direction, energy level, multimodal peak spectra, and different sea-swell combinations) cannot be comprehensively described by ξ; therefore, the reflective response of the RMB in different monsoonal seasons should be expressed using different prediction equations that are a function of ξ.

6. Summary and conclusion

The rubble mound breakwater (RMB) of Chabahar Bay along the northern coast of the Gulf of Oman serves as a crucial trade and connectivity spot in southern Iran. Seasonally reversing monsoonal winds influence the region's wave patterns, with southwestern winds prevailing during the summer monsoon (May to August) and northeasterly winds dominating the winter monsoon (November to February). Inter-monsoonal seasons – the pre-summer monsoon (March and April) and post-summer monsoon (September and October) – witness shifts in wind patterns and weather conditions, adding further complexity to the coastal dynamics of the area. The monthly and monsoonal variations of the reflective response of the RMB of Chabahar Bay have been investigated using directional wave data gathered employing an AWAC instrument adjacent to the breakwater.

The primary results show that the reflection coefficient K_r for swell waves is frequently higher than that of sea waves due to relatively more energy content dissipated after colliding of sea waves with RMB compared to more moderate breaking of swell waves with lower steepness. During the winter monsoon, when the region is subjected to a combination of moderate sea waves and weak swell waves approached from different incident directions, the scattering of K_r against Iribarren number ξ is reduced. Upon transition into the pre-summer monsoon months of March and April, the overall wave height and incident direction are similar to those of winter monsoon. Therefore, the reflective response of RMB closely resembles that of the winter monsoon.

The summer monsoon period from May to August is characterized by a persistent presence of highly energetic swell waves with sharp single-peaked energy spectra. In this period, only one significant wind source can be found, and sea and swell waves can only be distinguished by their different frequency bands. Despite the dominance of such high-energy swell waves generated by the strong southwest monsoon winds, there is an insignificant change in spectral period. The decrease in reflection coefficient values, coupled with energy dissipation due to intense wave breaking, leads to a significant dispersion in the reflective response of the RMB. Waves during the post-summer monsoon period have similar characteristics to those of summer monsoon with slight differences in the directions of sea and swell waves. Therefore, the post-summer monsoon period is practically a transition season from summer monsoon to winter monsoon with reduced scattering of reflective response compared with the summer monsoon period.

Power-and hyperbolic-law functions are used to predict wave reflection coefficient K_r in terms of Iribarren number ξ. Mean periods T_{m1} and T_{m2} and spectral peak period T_p separate data clouds of K_r against ξ into multiple groups and deteriorate the integrity of observations. This separation is particularly notable in bimodal wave energy spectra related to the combinations of sea-swell waves originating from different sources and directions. In contrast, employing the spectral periods T_{m-1} and T_{m-2} mitigates this separation and increases the accuracy of predictions. The comparison of monthly results of wave reflection obtained using the spectral periods T_{m-1} and T_{m-2} show that applying T_{m-2} significantly enhances the prediction accuracy for waves approaching from different directions with bimodal wave energy spectra, i.e., during the winter-monsoon and pre-summer monsoon periods. However, the reflection accuracy of waves with single-peak energy spectra with almost equal incident directions, i.e., during the summer and post-summer monsoon, show insignificant differences between T_{m-1} and T_{m-2}. It is also shown that using T_{m-2} increases the accuracy of the previous equations in predicting the observations of this study (Appendix A).

This study highlights different reflection performances of the RMB due to monsoonal changes in energy content and incident directions of sea and swell waves. Findings implicate that such variations are crucial for coastal structures and must be regarded when designing RBMs in regions affected by seasonal monsoons. However, further studies with longer-term field measurements could provide a more comprehensive understanding of the interannual variability and trends in wave dynamics and coastal processes. Additionally, three-dimensional experimental measurements with different bimodal wave spectra could provide accurate insight into the predictive performance of T_{m-2} in assessing the reflective behavior of coastal structures.

7. Data availability statement

The data that support the findings of this study are available from the corresponding author, upon reasonable request via m_mahmoudof@inio.ac.ir.

References

Aboobacker, V. M., Rashmi, R., Vethamony, P., Menon, H.B., 2011. *On the dominance of pre-existing swells over wind seas along the west coast of India*, Cont. Shelf. Res., 31(16), 1701–1712. https://doi.org/10.1016/j.csr.2011.07.010

Aboobacker, V.M., Shanas, P.R., 2018. *The climatology of shamals in the Arabian Sea – Part 1: Surface winds*, Int. J. Climatol. 38(12), 4405–4416. https://doi.org/10.1002/joc.5711

Altomare, C., Suzuki, T., Verwaest, T., 2020. *Influence of directional spreading on wave overtopping of sea dikes with gentle and shallow foreshores*. Coast. Eng. 157, 103654. https://doi.org/10.1016/j.coastaleng.2020.103654

Amrutha, M.M., Sanil Kumar, V., Sharma, S., Singh, J., Gowthaman, R., Kankara, R.S., 2015. *Characteristics of shallow water waves off the central west coast of India before, during and after the onset of the Indian summer monsoon*. Ocean Eng. 107, 259–270. https://doi.org/10.1016/j.oceaneng.2015.07.061

Andersen, T.L., 2006. *Hydraulic Response of Rubble Mound Breakwaters Scale Effects – Berm Breakwaters*. PhD Thesis, Hydraulics and Coastal Engineering Laboratory, Department of Civil Engineering, Aalborg University.

Aniel-Quiroga, Í., Vidal, C., Lara, J.L., González, M., 2019. *Pressures on a rubble-mound breakwater crown-wall for tsunami impact*. Coast. Eng. 152, 103522. https://doi.org/10.1016/j.coastaleng.2019.103522

Anoop, T.R., Shanas, P.R., Aboobacker, V.M., Kumar, V.S., Nair, L.S., Prasad, R., Reji, S., 2020. *On the generation and propagation of Makran swells in the Arabian Sea*. Int. J. Climatol. 40(1), 585–593. https://doi.org/10.1002/joc.6192

Barak, M.S., Kaliraman, V., 2019. *Reflection and transmission of elastic waves from an imperfect boundary between micropolar elastic solid half space and fluid saturated porous solid half space*. Mech. Adv. Mater. Struc. 26(14), 1226–1233. https://doi.org/10.1080/15376494.2018.1432795

Barak, M.S., Kumari, M., Kumar, M., 2018. *Effect of local fluid flow on the propagation of plane waves at an interface of water/double-porosity solid with underlying uniform elastic solid*. Ocean Eng. 147, 195–205. https://doi.org/https://doi.org/10.1016/j.oceaneng.2017.10.030

Battjes, J.A., 1974. *Surf Similarity*. 14th ASCE Coast. Eng. Conf., Copenhagen, Denmark.

Bourget, J., Zaragosi, S., Ellouz-Zimmermann, S., Ducassou, E., Prins, M. A., Garlan, T., Lanfumey, V., Schneider, J. L., Rouillard, P., and Giraudeau, J., 2010. *Highstand vs. lowstand turbidite system growth in the Makran active margin: Imprints of high-frequency external controls on sediment delivery mechanisms to deep water systems*. Mar. Geol. 274(1–4), 187–208. https://doi.org/10.1016/j.margeo.2010.04.005

Buccino, M., Calabrese, M., 2007. *Conceptual Approach for Prediction of Wave Transmission at Low-Crested Breakwaters*. J. Waterw. Port Coast. Ocean Eng. 133(3), 213–224. https://doi.org/doi:10.1061/(ASCE)0733-950X(2007)133:3(213)

Bruun, P., Gunbak, A.R., 1976. *New Design Principles for Rubble Mound Structures*. Coast. Eng. Proc. 1(15), 141. https://doi.org/10.9753/icce.v15.141

Calhoun, R.J., 1971 *Field study of wave transmission through a rubble-mound breakwater*. Master Thesis, Naval Postgraduate School, Monterey California, Publ. No. AD0721552. https://apps.dtic.mil/sti/citations/AD0721552

Cao, D., Tan, W., Yuan, J., 2022. *Assessment of wave overtopping risk for pedestrian visiting the crest area of coastal structure*. Appl. Ocean Res. 120, 102985. https://doi.org/10.1016/j.apor.2021.102985

Chaichitehrani, N., Allahdadi, M.N., 2018. *Overview of wind climatology for the Gulf of Oman and the northern Arabian Sea*. Am. J. Fluid Dynam. 8, 1–9.

Dattatri, J., Raman, H., Shankar, N.J., 1978. *Performance Characteristics of Submerged Breakwaters*. Coast. Eng. Proc., Hamburg, Germany.

Davidson, M.A., Bird, P.A.D., Bullock, G.N., Huntley, D.A., 1996. *A new non-dimensional number for the analysis of wave reflection from rubble mound breakwaters*. Coast. Eng. 28(1–4), 93–120. ttps://doi.org/10.1016/0378-3839(96)00012-9

Dekker, J., Caires, S., Van Gent, M.R.A., 2007. *Reflection of non-standard wave spectra by sloping structures*. 5th Coastal Structures International Conference, Venice, Italy.

Díaz-Carrasco, P., 2023. *Hydraulic performance analysis for homogeneous mound breakwaters: Application of dimensional analysis and a new experimental technique*. Ocean. Eng. 286(Pt. 2), 115598. https://doi.org/10.1016/J.OCEANENG.2023.115598

Díaz-Carrasco, P., Eldrup, M.R., Lykke Andersen, T., 2021. *Advance in wave reflection estimation for rubble mound breakwaters: The importance of the relative water depth*. Coast. Eng. 168, 103921. https://doi.org/10.1016/j.coastaleng.2021.103921

Dong, Y., Zheng, Z., Ma, Y., Gao, J., Ma, X., Dong, G., 2023. *Numerical investigation on the mitigation of harbor oscillations by periodic undulating topography*. Ocean Eng. 279, 114580.

Düing, W., 1970. *The Monsoon Regime of the Currents in the Indian Ocean*. East-West Center Press, Honolulu, 68 pp.

Eyhavand-Koohzadi, A., Badiei, P., 2021. *Laboratory experiments on time-space conversion of wind waves in deep water*. Appl. Ocean. Res. 111, 102656. https://doi.org/https://doi.org/10.1016/j.apor.2021.

102656

Eyhavand-Koohzadi, A., Badiei, P., 2022. *Experimental study on the growth and conversion of duration- and fetch-limited wind waves in water of finite depth*. Ocean. Eng. 266, 113020. https://doi.org/10.1016/j.oceaneng.2022.113020

Galiatsatou, P., Makris, C., Prinos, P., 2018. *Optimized Reliability Based Upgrading of Rubble Mound Breakwaters in a Changing Climate*. J. Mar. Sci. Eng. 6(3), 92. https://www.mdpi.com/2077-1312/6/3/92

Gao, J., Zhou, X., Zang, J., Chen, Q., Zhou, L., 2018. *Influence of offshore fringing reefs on infragravity period oscillations within a harbor*. Ocean Eng. 158, 286–298.

Gao, J., Zhou, X., Zhou, L., Zang, J., Chen, H., 2019. *Numerical investigation on effects of fringing reefs on low-frequency oscillations within a harbor*. Ocean Eng. 172, 86–95.

Gao, J., Ma, X., Dong, G., Chen, H., Liu, Q., Zang, J., 2021. *Investigation on the effects of Bragg reflection on harbor oscillations*. Coast. Eng. 170, 103977. https://doi.org/https://doi.org/10.1016/j.coastaleng.2021.103977

Gao, J., Shi, H., Zang, J., Liu, Y., 2023. *Mechanism analysis on the mitigation of harbor resonance by periodic undulating topography*. Ocean Eng. 281, 114923. https://doi.org/https://doi.org/10.1016/j.oceaneng.2023.114923

Gao, J., Hou, L., Liu, Y., Shi, H., 2024. *Influences of bragg reflection on harbor resonance triggered by irregular wave groups*. Ocean Eng. 305, 117941.

Goda, Y., 2010. *Random seas and design of maritime structures*. Adv. Ser. Ocean Eng. Vol. 33, World Sci., 732 pp.

Haider, R., Ali, S., Hoffmann, G., Reicherter, K., 2023. *A multi-proxy approach to assess tsunami hazard with a preliminary risk assessment: A case study of the Makran Coast, Pakistan*. Mar. Geol. 459, 107032. https://doi.org/10.1016/j.margeo.2023.107032

Han, X., Jiang, Y., Dong, S., 2022. *Wave forces on crown wall of rubble mound breakwater under swell waves*. Ocean. Eng. 259, 111911. https://doi.org/10.1016/j.oceaneng.2022.111911

Harry, M., Zhang, H., Lemckert, C., Colleter, G., Blenkinsopp, C., 2018. *Observation of surf zone wave transformation using LiDAR*. Appl. Ocean. Res. 78, 88–98. https://doi.org/10.1016/j.apor.2018.05.015

Hofland, B., Chen, X., Altomare, C., Oosterlo, P., 2017. *Prediction formula for the spectral wave period Tm-1,0 on mildly sloping shallow foreshores*. Coast. Eng. 123, 21–28. https://doi.org/10.1016/j.coastaleng.2017.02.005

Iglesias, G., Rabuñal, J., Losada, M.A., Pachón, H., Castro, A., Carballo, R., 2008. *A virtual laboratory for stability tests of rubble-mound breakwaters*. Ocean Eng. 35(11–12), 1113–1120. https://doi.org/10.1016/j.oceaneng.2008.04.014

Irías Mata, M., Van Gent, M.R.A., 2023. *Numerical modelling of wave overtopping discharges at rubble mound breakwaters using OpenFOAM®*. Coast. Eng. 181, 104274. https://doi.org/10.1016/j.coastaleng.2022.104274

Kamphuis, J.W., 2010. *Introduction to coastal engineering and management*. Adv. Ser. Ocean Eng. Vol. 30, World Sci., 564 pp.

Karnan, C., Gautham, S., 2023. *Seasonal enhancement of phytoplankton biomass in the southern tropical Indian Ocean: Significance of meteorological and oceanography parameters*. Oceanologia 66(2), 196–219. https://doi.org/10.1016/j.oceano.2023.10.003

Kober, F., Zeilinger, G., Ivy-Ochs, S., Dolati, A., Smit, J., and Kubik, P. W., 2013. *Climatic and tectonic control on fluvial and alluvial fan sequence formation in the Central Makran Range, SE-Iran*. Global Planet. Change 111, 133–149. https://doi.org/10.1016/j.gloplacha.2013.09.003

Koley, S., Panduranga, K., Almashan, N., Neelamani, S., and Al-Ragum, A., 2020. *Numerical and experimental modeling of water wave interaction with rubble mound offshore porous breakwaters*. Ocean. Eng. 218, 108218. https://doi.org/10.1016/j.oceaneng.2020.108218

Kor, K., Ershadifar, H., Ghazilou, A., and Koochaknejad, E., 2021. *Seasonal variations, potential bioavailability, and ecological risk of phosphorus species in the coastal sediments of the Makran*. Mar. Pollut. Bull. 173, 113125. https://doi.org/10.1016/j.marpolbul.2021.113125

Koutrouveli, T.I., Dimas, A.A., 2020. *Wave and hydrodynamic processes in the vicinity of a rubble-mound, permeable, zero-freeboard break water*. J. Mar. Sci. Eng. 8(3), 206. https://doi.org/10.3390/jmse8030206

Krishna, P.S., Aboobacker, V.M., Ramesh, M., Nair, L.S., 2023. *Remotely induced storm effects on the coastal flooding along the southwest coast of India*. Oceanologia 65(3), 503–516. https://doi.org/10.1016/j.oceano.2023.03.003

Kumar, R., Barak, M., 2007. *Wave propagation in liquid-saturated porous solid with micropolar elastic skelton at boundary surface*. Appl. Math. Mech. 28(3), 337–349. https://doi.org/10.1007/s10483-007-0307-z

Kumar, R., Gupta, V., Pathania, V., Kumar, R., Barak, M.S., 2023. *Analysis of Waves at Boundary Surfaces at Distinct Media with Nonlocal Dual-Phase-Lag*. Proceedings of the National Academy of Sciences, India Section A: Physical Sciences, 93(4), 573–585. https://doi.org/10.1007/s40010-023-00850-y

Lahiri, S.P., Vissa, N.K., 2022. *Assessment of Indian Ocean upwelling changes and its relationship with the Indian monsoon*. Global Plant. Change 208, 103729. https://doi.org/https://doi.org/10.1016/j.gloplacha.2021.103729

Lee, J.I., Shin, S., 2014. *Experimental study on the wave reflection of partially perforated wall caissons with single and double chambers*. Ocean. Eng. 91, 1–10. https://doi.org/10.1016/j.oceaneng.2014.08.008

Li, A.J., Liu, Y., Fang, H., Liu, X., 2022. *Wave scattering by a periodic array of porous breakwaters*. Appl. Ocean Res. 127, 103328. https://doi.org/10.1016/j.apor.2022.103328

Li, D., Anis, A., Al Senafi, F., 2020. *Physical response of the Northern Arabian Gulf to winter Shamals*. J. Marine Syst. 203, 103280. https://doi.org/10.1016/j.jmarsys.2019.103280

Liu, Y., Li, S., Chen, S., Hu, C., Fan, Z., Jin, R., 2020. *Random wave overtopping of vertical seawalls on coral reefs*. Appl. Ocean Res. 100, 102166. https://doi.org/https://doi.org/10.1016/j.apor.2020.102166

Liu, Y., Li, S., Liao, Z., Liu, K., 2021. *Physical and numerical modeling of random wave transformation and overtopping on reef topography*. Ocean Eng. 220, 108390. https://doi.org/https://doi.org/10.1016/j.oceaneng.2020.108390

Losada, M.A., Giménez-Curto, L.A., 1980. *Flow characteristics on rough, permeable slopes under wave action*. Coast. Eng. 4, 187–206. https://doi.org/10.1016/0378-3839(80)90019-8

Lykke Andersen, T., Burcharth, H.F., 2009. *Three-dimensional investigations of wave overtopping on rubble mound structures*. Coast. Eng. 56(2), 180–189. https://doi.org/https://doi.org/10.1016/j.coastaleng.2008.03.007

Mahmoudof, S.M., Azizpour, J., 2020. *Field observation of wave reflection from plunging cliff coasts of Chabahar*. Appl. Ocean. Res. 95, 102029–102029. https://doi.org/10.1016/J.APOR.2019.102029

Mahmoudof, S.M., Hajivalie, F., 2021. *Experimental study of hydraulic response of smooth submerged breakwaters to irregular waves*. Oceanologia 63(4), 448–462. https://doi.org/10.1016/j.oceano.2021.05.002

Mahmoudof, S.M., Azizpour, J., Eyhavand-Koohzadi, A., 2021a. *Observation of infragravity wave processes near the coastal cliffs of Chabahar (Gulf of Oman)*. Estuar. Coast. Shelf Sci. 251, 107226. https://doi.org/10.1016/j.ecss.2021.107226

Mahmoudof, S.M., Eyhavand-Koohzadi, A., Bagheri, M., 2021b. *Field study of wave reflection from permeable rubble mound breakwater of Chabahar Port*. Appl. Ocean Res. 114, 102786–102786. https://doi.org/10.1016/J.APOR.2021.102786

Mahmoudof, S.M., Siadatmousavi, S.M., Seyedalipour, S.A., 2021c. *Experimental study of bound triad interactions across a dissipative surf zone under different wave breaking conditions*. Ocean Eng. 235, 109427. https://doi.org/10.1016/j.oceaneng.2021.109427

Mahmoudof, S.M., Takami, M.L., 2022. *Numerical study of coastal wave profiles at the sandy beaches of Nowshahr (Southern Caspian Sea)*. Oceanologia 64(3), 457–472. https://doi.org/https://doi.org/10.1016/j.oceano.2022.03.001

Mahmoudof, S.M., Eyhavand-Koohzadi, A., Kazeminezhad, M.H., 2023. *Field investigation of spectral wave period $T_{m-1,0}$ on shallow and very shallow foreshores of the southern Caspian Sea*. Coast. Eng. 181, 104277. https://doi.org/10.1016/j.coastaleng.2023.104277

Masselink, G., 1998. *Field investigation of wave propagation over a bar and the consequent generation of secondary waves*. Coast. Eng. 33(1), 1–9. https://doi.org/https://doi.org/10.1016/S0378-3839(97)00032-X

Morrison, J.M., Codispoti, L.A., Gaurin, S., Jones, B., Manghnani, V., Zheng, Z., 1998. *Seasonal variation of hydrographic and nutrient fields during the US JGOFS Arabian Sea Process Study*. Deep-Sea Res. Pt. II 45(10–11), 2053–2101. https://doi.org/10.1016/S0967-0645(98)00063-0

Mostaghiman, A., Moghim, M.N., 2022. *An experimental study of partly/hardly reshaping mass-armored double-berm breakwaters*. Ocean Eng. 243, 110258. https://doi.org/10.1016/j.oceaneng.2021.110258

Muttray, M., Oumeraci, H., Oever, E.T., 2006. *Wave reflection and wave run-up at rubble mound breakwaters*. 30th International Conference, San Diego, California, USA.

Myrhaug, D., 2020. *Some probabilistic properties of surf parameter*. Oceanologia 62(3), 395–401. https://doi.org/10.1016/j.oceano.2020.02.003

Nassar, K., Mahmod, W.E., Tawfik, A., Rageh, O., Negm, A., and Fath, H., 2018. *Developing empirical formulas for assessing the hydrodynamic behaviour of serrated and slotted seawalls*. Ocean Eng. 159, 388–409. https://doi.org/10.1016/j.oceaneng.2018.04.048

Neelamani, S., Al-Salem, K., Rakha, K., 2007. *Extreme waves for Kuwaiti territorial waters*. Ocean Eng. 34(10), 1496–1504. https://doi.org/10.1016/j.oceaneng.2006.08.013

Nguyen, N.M., Van, D.D., Le, D.T., Cong, S.D., Pham, N.T., Nguyen, Q., Tran, B., Wright, D.P., Tanim, A.H., Anh, D.T., 2022. *Wave reduction efficiency for three classes of breakwaters on the coastal Mekong Delta*. Appl. Ocean. Res. 129, 103362. https://doi.org/10.1016/j.apor.2022.103362

Numata, A., 1976. *Laboratory Formulation For Transmission And Reflection At Permeable Breakwaters Of Artificial Blocks*. Coast. Eng. Japan 19(1), 47–58. https://doi.org/10.1080/05785634.1976.11924216

Oumeraci, H., Partenscky, H.W., 1990. *Wave-Induced Pore Pressure in Rubble Mound Breakwaters*. 22nd International Conference on Coastal Engineering, Delft, The Netherlands, July 2–6, 1990, 1334–1347. https://doi.org/doi:10.1061/9780872627765.102

Peihong, Z., Dapeng, S., Hao, W., Yucheng, L., 2021. *Theoretical investigation of wave reflection from partially perforated caisson sitting on a rubble mound foundation*. Ocean Eng. 235, 109085. https://doi.org/10.1016/j.oceaneng.2021.109085

Pedersen, T., Lohrmann, A., 2004. *Possibilities and limitations of acoustic surface tracking*. Oceans '04 MTS/IEEE Techno-Ocean '04 (IEEE Cat. No.04CH37600), Kobe, Japan.

Pedersen, T., Siegel, E., Wood, J., 2007. *Directional Wave Measurements from a Subsurface Buoy with an Acoustic Wave and Current Profiler (AWAC)*. Oceans 2007, Vancouver, BC, Canada.

Postma, G.M., 1989. *Wave reflection from rock slopes under random wave attack*. Master thesis, University of Technology Delft. http://resolver.tudelft.nl/uuid:4c21a913-a78b-40d2-b690-a0184683434b

Pratola, L., Rinaldi, A., Molfetta, M.G., Bruno, M.F., Pasquali, D., Dentale, F., Mossa, M., 2021. *Investigation on the reflection coefficient for seawalls protected by a rubble mound structure*. J. Mar. Sci. Eng. 9, 937. https://doi.org/10.3390/jmse9090937

Prizomwala, S.P., Vedpathak, C., Tandon, A., Das, A., Makwana, N., Joshi, N., 2022. *Geological footprints of the 1945 Makran tsunami from the west coast of India*. Mar. Geol. 446(106773). https://doi.org/10.1016/j.margeo.2022.106773

Radfar, S., Shafieefar, M., Akbari, H., Galiatsatou, P.A., Mazyak, A.R., 2021. *Design of a rubble mound breakwater under the combined effect of wave heights and water levels, under present and future climate conditions*. Appl. Ocean Res. 112, 102711. https://doi.org/10.1016/j.apor.2021.102711

Requejo, S., Vidal, C., and Losada, I.J., 2002. *Modelling of wave loads and hydraulic performance of vertical permeable structures*. Coast. Eng. 46(4), 249–276. https://doi.org/10.1016/S0378-3839(02)00072-8

Saket, A., Etemad-Shahidi, A., 2012. *Wave energy potential along the northern coasts of the Gulf of Oman, Iran*. Renew. Energ. 40(1), 90–97. https://doi.org/10.1016/j.renene.2011.09.024

Salauddin, M., Pearson, J.M., 2020. *Laboratory investigation of overtopping at a sloping structure with permeable shingle foreshore*. Ocean. Eng. 197, 106866. https://doi.org/10.1016/j.oceaneng.2019.106866

Samiksha, S.V., Vinodkumar, K., Vethamony, P., 2014. *Impact of shamal winds and swells on the coastal currents along the west coast of India*. Indian J. Geo.-Mar. Sci. 43(7), 1236–1240.

Sanil Kumar, V., Singh, J., Pednekar, P., Gowthaman, R., 2011. *Waves in the nearshore waters of northern Arabian Sea during the summer monsoon*. Ocean. Eng. 38(2–3), 382–388. https://doi.org/https://doi.org/10.1016/j.oceaneng.2010.11.009

Seelig, W.N., Ahrens, J.P., 1981. *Estimation of wave reflection and energy dissipation coefficients for beaches, revetments, and breakwaters*. U.S. Army Coastal Engineering Research Center Technical Paper, 81-1.

Shamji, V.R., 2021. *Beach classifications in response to southwest monsoon waves: A case study*. Indian J. Geo.-Mar. Sci. 50, 14–20. http://nopr.niscpr.res.in/handle/123456789/56099

Shankar, D., Vinayachandran, P.N., Unnikrishnan, A.S., 2002. *The monsoon currents in the north Indian Ocean*. Prog. Oceanogr. 52(1), 63–120. https://doi.org/https://doi.org/10.1016/S0079-6611(02)00024-1

Sierra, J.P., 2019. *Economic Impact of Overtopping and Adaptation Measures in Catalan Ports Due to Sea Level Rise*. Water 11(7), 1440. https://www.mdpi.com/2073-4441/11/7/1440

Sinha, M., Jha, S., Chakraborty, P., 2020. *Indian Ocean wind speed variability and global teleconnection patterns*. Oceanologia 62(2), 126–138. https://doi.org/10.1016/j.oceano.2019.10.002

Smith, S. L., Criales, M.M., Schack, C., 2020. *The large-bodied copepods off Masirah Island, Oman: An investigation of Southwest Monsoon onset and die-off*. J. Marine Syst. 204, 103289. https://doi.org/https://doi.org/10.1016/j.jmarsys.2019.103289

Smitha, A., Sankar, S., Satheesan, K., 2023. *Impact of tropical Indian Ocean warming on the surface phytoplankton biomass at two significant coastal upwelling zones in the Arabian Sea*. Dynam. Atmos. Oceans 104, 101401. https://doi.org/https://doi.org/10.1016/j.dynatmoce.2023.101401

Sollitt, C.K., Cross, R.H., 1972. *Wave Transmission through Permeable Breakwaters*. 13th Conference on Coastal Engineering, Vancouver, Canada.

Sreelakshmi, S., Bhaskaran, P.K., 2020. *Wind-generated wave climate variability in the Indian Ocean using ERA-5 dataset*. Ocean Eng. 209, 107486. https://doi.org/10.1016/j.oceaneng.2020.107486

Stagnitti, M., Lara, J.L., Musumeci, R.E., Foti, E., 2023. *Numerical Modeling of Wave Overtopping of Damaged And Upgraded Rubble-Mound Breakwaters*. Ocean Eng. 280, 114798. https://doi.org/https://doi.org/10.1016/j.oceaneng.2023.114798

Sulisz, W., McDougal, W.G., Sollitt, C.K., 1989. *Wave interaction with rubble toe protection*. Ocean Eng. 16(5–6), 463–473. https://doi.org/10.1016/0029-8018(89)90047-4

Uścinowicz, G., Uścinowicz, S., Szarafin, T., Maszloch, E., Wirkus, K., 2023. *Rapid coastal erosion, its dynamics and cause–an erosional hot spot on the southern Baltic Sea coast*. Oceanologia 66(2), 250–266.

https://doi.org/10.1016/j.oceano.2023.12.002

Van der Meer, J.W., 1992. *Conceptual Design of Rubble Mound Breakwaters*. Design and Reliability of Coastal Structures, 23rd ICCE in Venice, Venice, Italy.

Van der Meer, J.W., 1997. *Golfoploop en golfoverslag bij dijken*. Hydraulic Engineering Reports, H2458/H3051, Delft Hydraulics, The Netherlands.

Van der Meer, J.W., Briganti, R., Zanuttigh, B., Wang, B., 2005. *Wave transmission and reflection at low-crested structures: Design formulae, oblique wave attack and spectral change*. Coast. Eng. 52(10–11), 915–929. https://doi.org/10.1016/j.coastaleng.2005.09.005

Van der Meer, J.W., Daemen, I.F.R., 1994. *Stability and Wave Transmission at Low-Crested Rubble-Mound Structures*. J. Waterw. Port Coast. Ocean Eng. 120(1). https://doi.org/10.1061/(asce)0733-950x(1994)120:1(1)

Van Gent, M.R.A., 1999. *Wave run-up and wave overtopping for double peaked wave energy spectra*. Hydraulic Engineering Reports, No. H3351, University of Technology, Delft, The Netherlands.

Van Gent, M.R.A., 2001. *Wave Runup on Dikes with Shallow Foreshores*. J. Waterw. Port Coast. Ocean Eng. 127(5), 254–262. https://doi.org/doi:10.1061/(ASCE)0733-950X(2001)127:5(254)

Van Gent, M.R.A., Buis, L., Van den Bos, J.P., Wüthrich, D., 2023. *Wave transmission at submerged coastal structures and artificial reefs*. Coast. Eng. 184, 104344. https://doi.org/10.1016/j.coastaleng.2023.104344

Vinod Kumar, K., Seemanth, M., Vethamony, P., Aboobacker, V.M., 2014. *On the spatial structure and time evolution of shamal winds over the Arabian Sea - a case study through numerical modelling*. Int. J. Climatol. 34(6), 2122–2128. https://doi.org/10.1002/joc.3819

Wang, Y., Jiang, D., Li, Y., 2022. *Numerical research of harbor oscillation influenced by vegetation*. Ocean Eng. 244, 110255.

Wilson, K.W., Cross, R.H., 1972. *Scale Effects In Rubble-Mound Breakwaters*. 13th Conference on Coastal Engineering, Vancouver, Canada.

Zanuttigh, B., Van der Meer, J.W., 2008. *Wave reflection from coastal structures in design conditions*. Coast. Eng. 55(10), 771–779. https://doi.org/10.1016/j.coastaleng.2008.02.009

Zanuttigh, B., Van der Meer, J.W., Andersen, T.L., Lara, J.L., Losada, I.J., 2008. *Analysis of wave reflection from structures with berms through an extensive database and 2DV numerical modelling*. 31st International Conference of Coastal Engineering, Hamburg, Germany.

Zhang, Y., Li, M., Zhao, X., Chen, L., 2020. *The effect of the coastal reflection on the performance of a floating breakwater-WEC system*. Appl. Ocean. Res. 100, 102117. https://doi.org/10.1016/j.apor.2020.102117

Zhao, W., Wei, K., Zhong, X., 2023. *Estimation of breaking wave region based on coupled wave and storm surge simulations of historical typhoons: A case study of Hangzhou Bay*. Ocean. Eng. 286 (Part 1), 115596. https://doi.org/10.1016/J.OCEANENG.2023.115596

Zhao, Z., Wu, W., Wang, M., Du, Y., 2023. *Circulation structure and dynamic characteristics of Western Tropical Indian Ocean associated with monsoon transitions*. Deep-Sea Res. Pt. I 191, 103943. https://doi.org/10.1016/j.dsr.2022.103943

Appendix A: Evaluation of previous prediction formulae

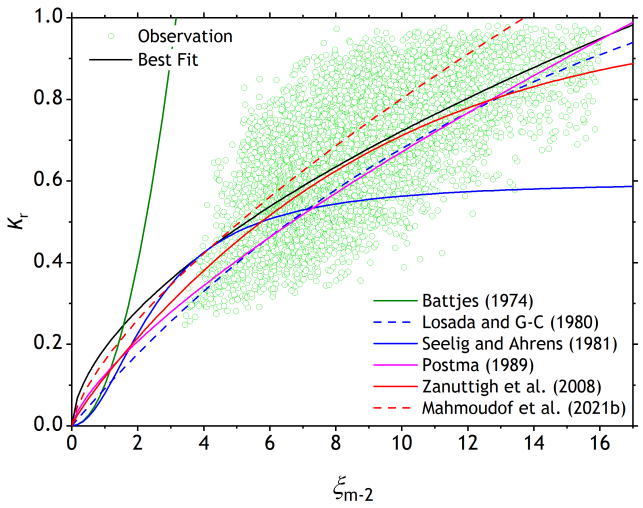

Figure A1. Scatter plots of reflection coefficient K_r for the bulk observations against Iribarren number ξ_{m-2}. Best-fitted power-law equation (black solid line) is Eq. (A1), while the equations of other curves are presented in Table 1.

While the difference in the reflective response of RMB during summer- and winter monsoon periods has been demonstrated in Section 4, the prediction of the reflection coefficient for the bulk (entire year) data has been provided here. In Figure A1, all measurements conducted in this study (7112 seasonally unclassified points) are depicted. Since it is shown that using ξ_{m-2} predicts K_r values more accurately (especially during winter-monsoon seasons), only observations scaled with this parameter are displayed in the figure. Also, the best fit performed on this data and the predictions of previously suggested functions are shown (see Table 1). The best-fit power law over the bulk observations, which gives $R^2 = 0.51$, shown in Figure A1, is:

$$K_r = 0.17\xi_{m-2}^{0.63} \tag{A1}$$

Figure A2 categorizes the data presented in Figure A1 based on monsoonal seasons, along with the best-fitted and preexisting prediction functions. Finally, Table A1 compares the performance of all predictive equations shown in Figures A1 and A2 based on the R^2 parameter. In this table, the effect of scaling by the spectral periods T_{m-1} and T_{m-2} over the prediction accuracy of the bulk and seasonally categorized data is also compared.

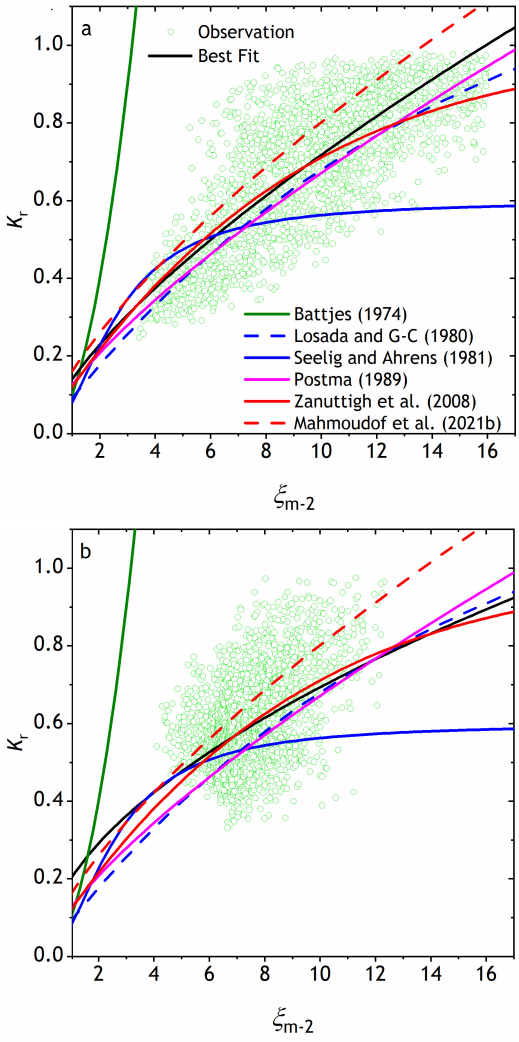

Figure A2. Scatter plots of reflection coefficient K_r against Iribarren number ξ_{m-2} during winter-monsoon seasons (panel a) and summer monsoon seasons (panel b). Best-fitted power laws (black solid lines) are Eq. (9) (panel a) and Eq. (11) (panel b), while the equations of other curves are presented in Table 1.

Table A1. The values of R^2 for power laws scaled by ξ_{m-1} and ξ_{m-2} fitted over summer monsoon, winter monsoon, and bulk measurements. The negative R^2 values are not presented.

		This study	Battjes (1974)	Losada and Giménez-Curto (1980)	Seelig and Ahrens (1981)	Postma (1989)	Zanuttigh et al. (2008)
Winter	ξ_{m-1}	0.56	–	0.13	–	0.11	0.39
	ξ_{m-2}	0.65	–	0.58	–	0.57	0.62
Summer	ξ_{m-1}	0.20	–	–	–	–	–
	ξ_{m-2}	0.23	–	–	–	–	0.20
Bulk data	ξ_{m-1}	0.47	–	–	–	–	0.30
	ξ_{m-2}	0.51	–	0.35	–	0.32	0.50